Electronic Supplementary Information

Boosting NH_3 production from nitrate electroreduction via electronic structure engineering of Fe_3C nanoflakes

Yuanyuan Wang,[a] Linlin Zhang,[a*] Yongjian Niu,[a] Dong Fang,[a] Jiao Wang,[a] Qingxiao Su[a] and Cheng Wang[a]

[a] Tianjin Key Laboratory of Advanced Functional Porous Materials
Institute for New Energy Materials and Low-Carbon Technologies
School of Material Science and Engineering
Tianjin University of Technology
Tianjin 300384, People's Republic of China

[*] Corresponing author: Linlin Zhang; Email: zhanglinlin_cn@126.com

Table of contents

The equations involved in this work are listed as follows:

$\varepsilon_d = \int_{-\infty}^{\infty} n_d(\varepsilon)\varepsilon d\varepsilon / \int_{-\infty}^{\infty} n_d(\varepsilon)\, d\varepsilon$ (1) , where ε_d is the d-band center, ε is the energy relative to the fermi level and $n_d(\varepsilon)$ is the phtotoelectron intensity after the subtraction of the shirley-type background. The upper level of the integration was fixed at 8.0 eV for accurate comparison.

$\Phi = 21.2 - SEE$ (2), where Φ is the work function and SEE is the binding energy corresponding to the secondary electron cutoff edge.

E (*vs*. RHE) = E (*vs*. Hg/HgO) + 0.059 × pH + 0.098 (3), where E (*vs*. RHE) and E (*vs*. Hg/HgO) are the applied potentials relative to the reversible hydrogen electrode and to the Hg/HgO electrode, respectively.

$Y_{NH3} = C(NH_3)\times V/(t\times m_{cat.})$ (4), $FE_{NH3} = 8F\times C(NH_3)\times V/(17Q)\times 100\%$ (5), and $J_{NH3} = (I\times FE_{NH3})/A$ (6), where Y_{NH3}, FE_{NH3} and J_{NH3} are the yield, faradaic efficiency and partial current density of NH_3, respectively; $C(NH_3)$ is the molar concentration of measured NH_3, V is the volume of the electrolyte, t is the electrolysis time, $m_{cat.}$ is the mass of the loaded catalyst, F is the Faraday constant (96485 C mol^{-1}) and Q is the total charge passing through the electrode ($Q = \int_0^t jdt$, j is the geometric current density), I is the current during the constant potential electrolysis, A is the surface area of the cathode.

Selec. = $C(NH_3)/\Delta C(NO_3^-)\times 100\%$ (7), where Selec. is the selectivity of NH_3, C_0 is the initial concentration of NO_3^- in the electrolyte and $\Delta C(NO_3^-)$ is the concentration difference of NO_3^- before and after electrolysis

$EE_{NH3} = (1.23-E^0_{NH3})FE_{NH3}/(1.23-E)$ (8), where EE_{NH3} is the energy efficiency for nitrate electroreduction to ammonia, E^0_{NH3} is the equilibrium potential of nitrate electroreduction to ammonia (0.69 V), FE_{NH3} is the faradaic efficiency for ammonia, 1.23 V is the equilibrium potential of water oxidation and E is the applied potential *vs*. RHE.

$Y_{NO2-} = C(NO_2^-)\times V/(t\times m_{cat.})$ (9), $FE_{NO2-} = 2F\times C(NO_2^-)\times V/(46Q)\times 100\%$ (10), where Y_{NO2-} and FE_{NO2-} are the yield and faradaic efficiency of NO_2^-, respectively; $C(NO_2^-)$ is the molar concentration of measured NO_2^-, V is the volume of the electrolyte, t is the electrolysis time, $m_{cat.}$ is the mass of the loaded catalyst, F is the Faraday constant (96485 C mol^{-1}) and Q is the total charge passing through the electrode ($Q = \int_0^t jdt$, j is the geometric current density).

$Y_{N2H4} = C(N_2H_4)\times V/(t\times mcat.)$ (11), $FE_{N2H4} = 7F\times C(N_2H_4)\times V/(32Q)\times 100\%$ (12), where Y_{N2H4} and

FE_{N2H4} are the yield and faradaic efficiency of N_2H_4, respectively; $C(NO_2^-)$ is the molar concentration of measured NO_2^-, V is the volume of the electrolyte, t is the electrolysis time, $m_{cat.}$ is the mass of the loaded catalyst, F is the Faraday constant (96485 C mol^{-1}) and Q is the total charge passing through the electrode ($Q = \int_0^t jdt$, j is the geometric current density).

$E = a + blog(J_{NH3})$ (13), where E is the applied potential *vs*. RHE, J_{NH3} is the partial current density of NH_3, a is a constant and b is the Tafel slope

$ln(C_0/C_t) = k_{ap}t$ (14), where k_{ap} is the apparent rate constant, C_0 and C_t are the concentrations of NO_3^- in the electrolytes at the beginning and at reaction time t, respectively

$1/r_0 = 1/(kK_{ads}C_0) + 1/k$ (15), where K_{ads} is the equilibrium adsorption constants for NO_3^-, r_0 is the initial reduction rate of NO_3^- ($r_0 = k_{ap}C_0$), k is the rate constant for the adsorbed NO_3^-, C_0 is the initial concentration of NO_3

$\Delta G_{ads} = -RTlnK_{ads}$ (16), where ΔG_{ads} is the adsorption free energy of NO_3^-, R is the gas constant, T is the reaction temperature and K_{ads} is the equilibrium adsorption constants for nitrate ions.

$i_k = Ae^{(-Ea/RT)}$ (17), where E_a is the apparent activation energy, i_k is the kinetic current at -0.5 V, A is the pre-exponential factor, T is the reaction temperature and R is the universal gas constant

$j_p = (-2.99\times10^5)n\alpha^{1/2}CD^{1/2}\nu^{1/2}$ (18), where n is the charge transfer number, j_p is the peak current density (A cm^{-2}), α is transfer coefficient (0.5), C is the nitrate concentration in electrolytes (7.5×10^{-5} mol cm^{-3}), D is the diffusion coefficient of nitrate ions (2.0×10^{-5} cm^2 s^{-1}) and ν is the scan rate (V s^{-1}).

Figure S1. Photographs for the Fe-NTA mixture (a), Fe-NTA precursor (b), Fe-NTA complex (c) and Fe_3C/NC (d).

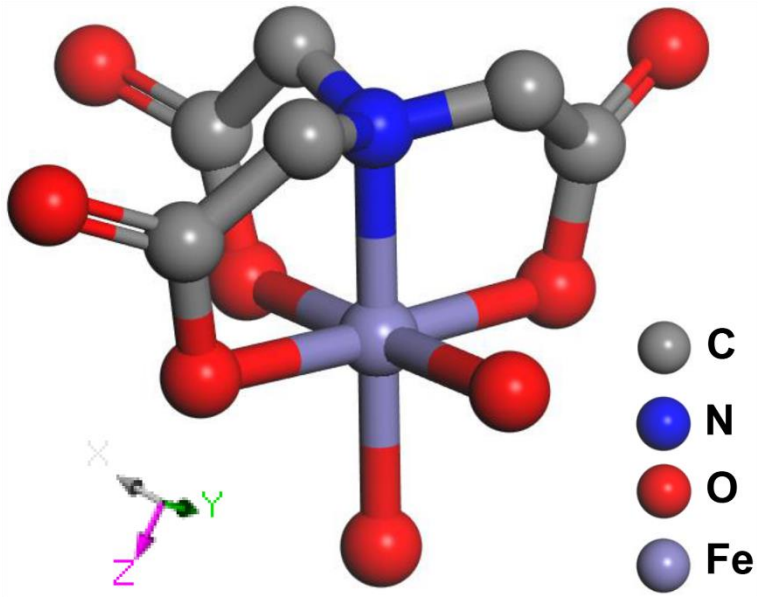

Figure S2. The possible crystal structure of the Fe-NTA complex.

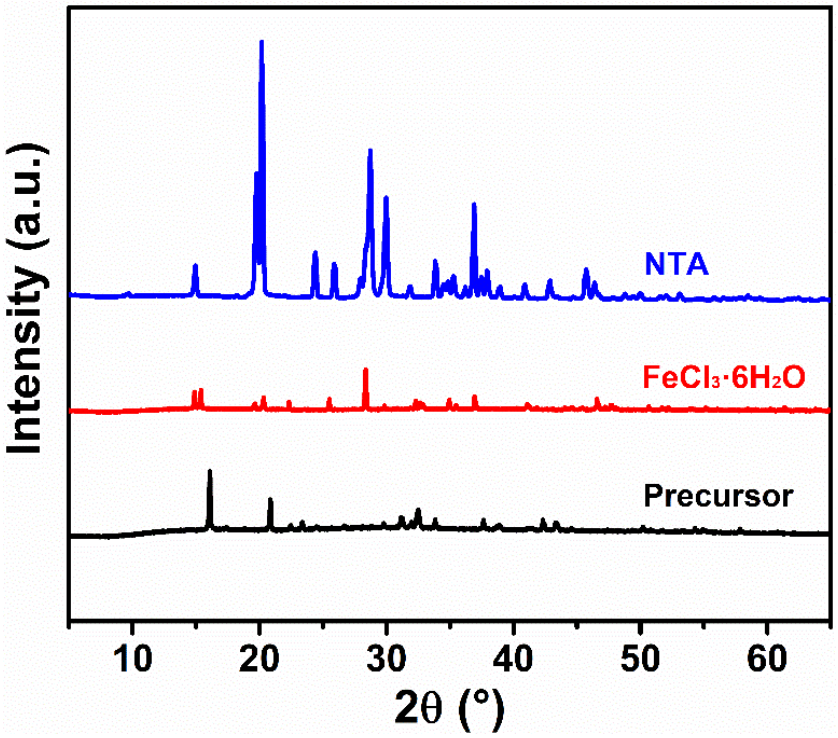

Figure S3. XRD patterns of NTA, $FeCl_3 \cdot 6H_2O$ and the Fe-NTA complex.

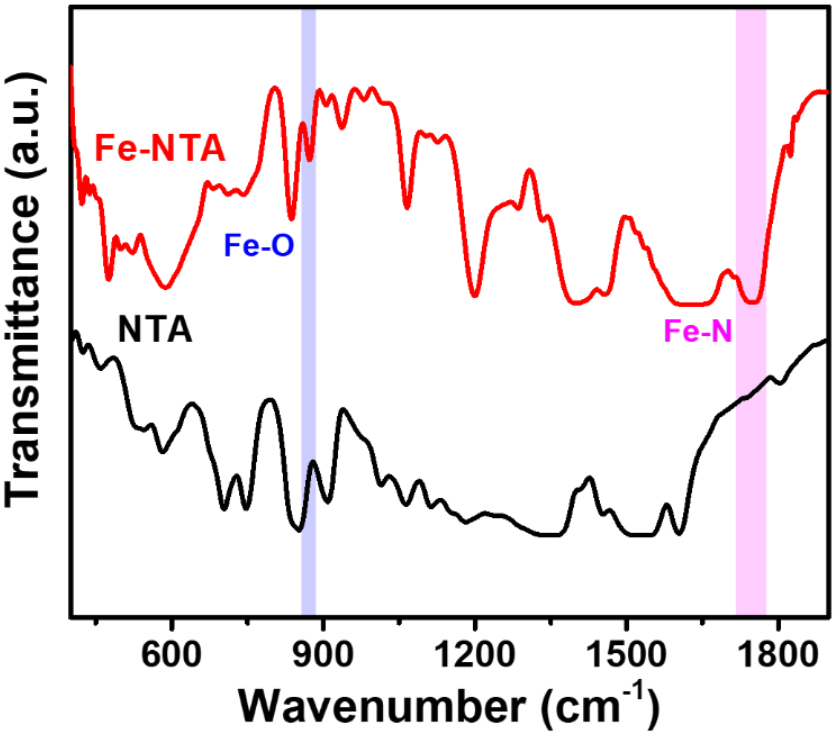

Figure S4. FTIR spectra of the Fe-NTA complex (red) and pure NTA (black). The peaks located at about 850 cm^{-1} and 1770 cm^{-1} were assigned to the vibrations of Fe-O and Fe-N bonds, respectively.

Table S1. Summary of the synthetic conditions for the control samples in this work

Entry	Sample	Solvothermal				Calcination			Etching	Post treatment
		n(Fe) (mmol)	n(NTA) (mmol)	Temp. (℃)	Time (h)	Temp. (℃)	Time (h)	Rate (℃ min^{-1})	C(HCl) (M)	Temp. (℃)
1	Fe_3C/NC	4	2	180	6	700	2	2	2	-
2	Fe_3C/NC-0.5Fe	2	2	180	6	700	2	2	2	-
3	Fe_3C/NC-2Fe	8	2	180	6	700	2	2	2	-
4	Fe_3C/NC-0.5C	2	1	180	6	700	2	2	2	-
5	Fe_3C/NC-2C	8	4	180	6	700	2	2	2	-
6	Fe_3C/NC-2NTA	4	4	180	6	700	2	2	2	-
7	Fe_3C/NC-0.5NTA	4	4	180	6	700	2	2	2	-
8	Fe_3C/NC-140	4	2	140	6	700	2	2	2	-
9	Fe_3C/NC-220	4	2	220	6	700	2	2	2	-
10	Fe_3C/NC-3h	4	2	180	3	700	2	2	2	-
11	Fe_3C/NC-9h	4	2	180	9	700	2	2	2	-
12	Fe_3C/NC-600	4	2	180	6	600	2	2	2	-
13	Fe_3C/NC-650	4	2	180	6	650	2	2	2	-
14	Fe_3C/NC-750	4	2	180	6	750	2	2	2	-
15	Fe_3C/NC-800	4	2	180	6	800	2	2	2	-
16	Fe_3C/NC-1R	4	2	180	6	700	2	1	2	-
17	Fe_3C/NC-5R	4	2	180	6	700	2	5	2	-
18	Fe_3C/NC-0.5H	4	2	180	6	700	0.5	2	2	-
19	Fe_3C/NC-4H	4	2	180	6	700	4	2	2	-
20	NC[a]	4	2	180	6	700	2	2	12	-
21	NC-600[a]	4	2	180	6	600	2	2	12	-
22	NC-800[a]	4	2	180	6	800	2	2	12	-
23	H_2-100[b]	4	2	180	6	700	2	2	2	100
24	H_2-300[b]	4	2	180	6	700	2	2	2	300
25	Air-100[c]	4	2	180	6	700	2	2	2	100
26	Air-200[c]	4	2	180	6	700	2	2	2	200

[a] NC, NC-600 and NC-800 were synthesized using a 12 M concentrated HCl solution in the etching process under otherwise identical conditions with Fe_3C/NC, Fe_3C/NC-600 and Fe_3C/NC-800, respectively.

[b] H_2-100 and H_2-300 were prepared by heating Fe_3C/NC under H_2/Ar at 100 and 300 ℃ for 2 h, respectively.

[c] Air-100 and Air-200 were prepared by heating Fe_3C/NC in air at 100 and 200 ℃ for 2 h, respectively.

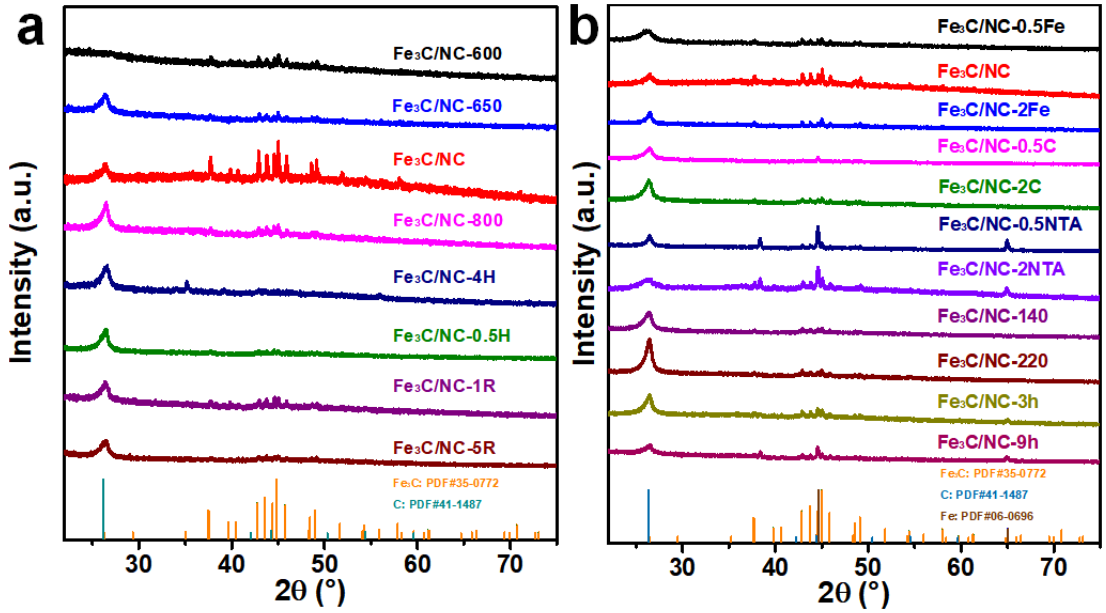

Figure S5. XRD patterns of samples prepared under different annealing (a) and solvothermal (b) conditions. All samples possessed similar compositions with Fe_3C/NC except for Fe_3C/NC-0.5NTA, Fe_3C/NC-2NTA, Fe_3C/NC-3h and Fe_3C/NC-9h, which contained additional species of metallic Fe.

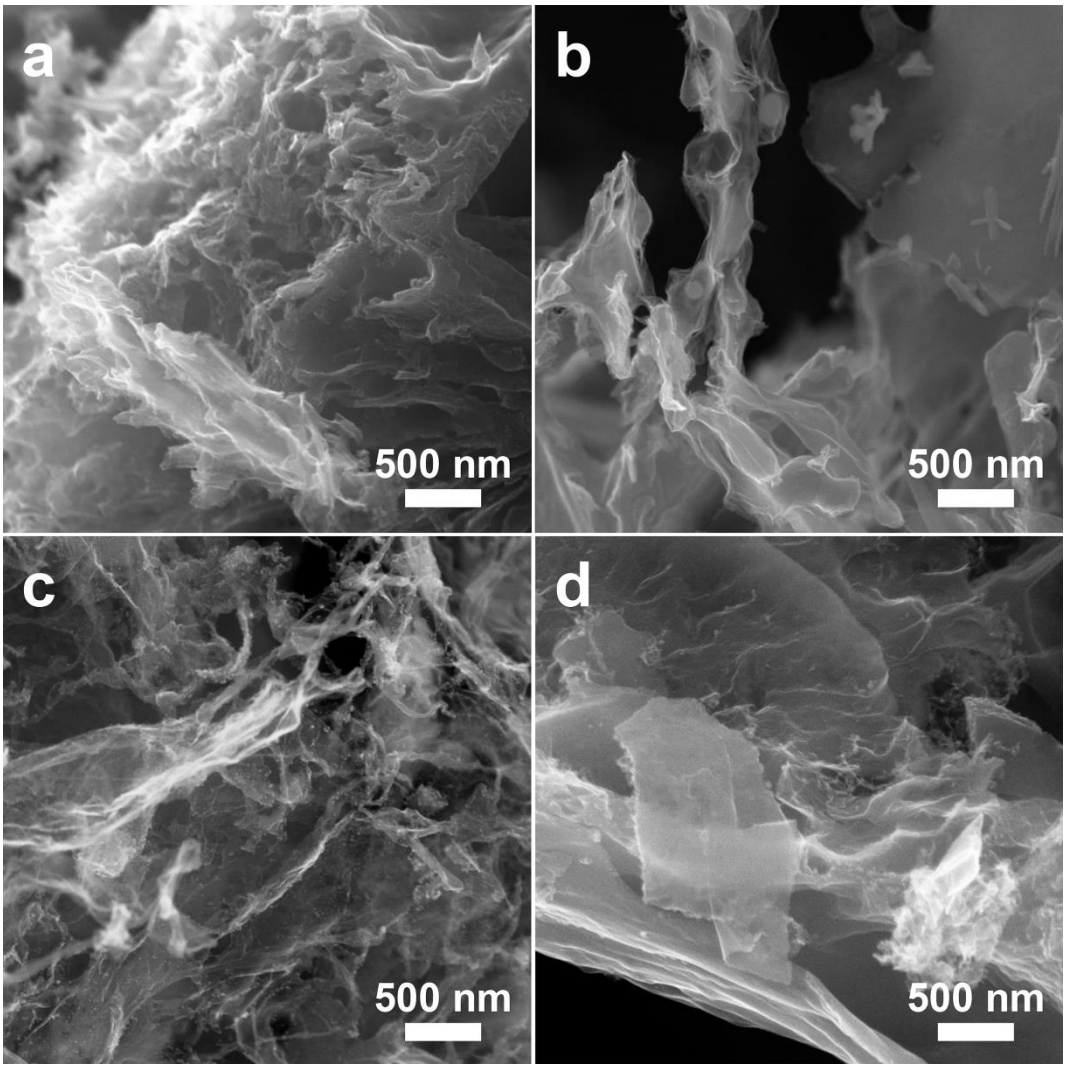

Figure S6. SEM images for samples prepared at different annealing temperatures. (a) Fe_3C/NC-600, (b) Fe_3C/NC-650, (c) Fe_3C/NC, (d) Fe_3C/NC-800.

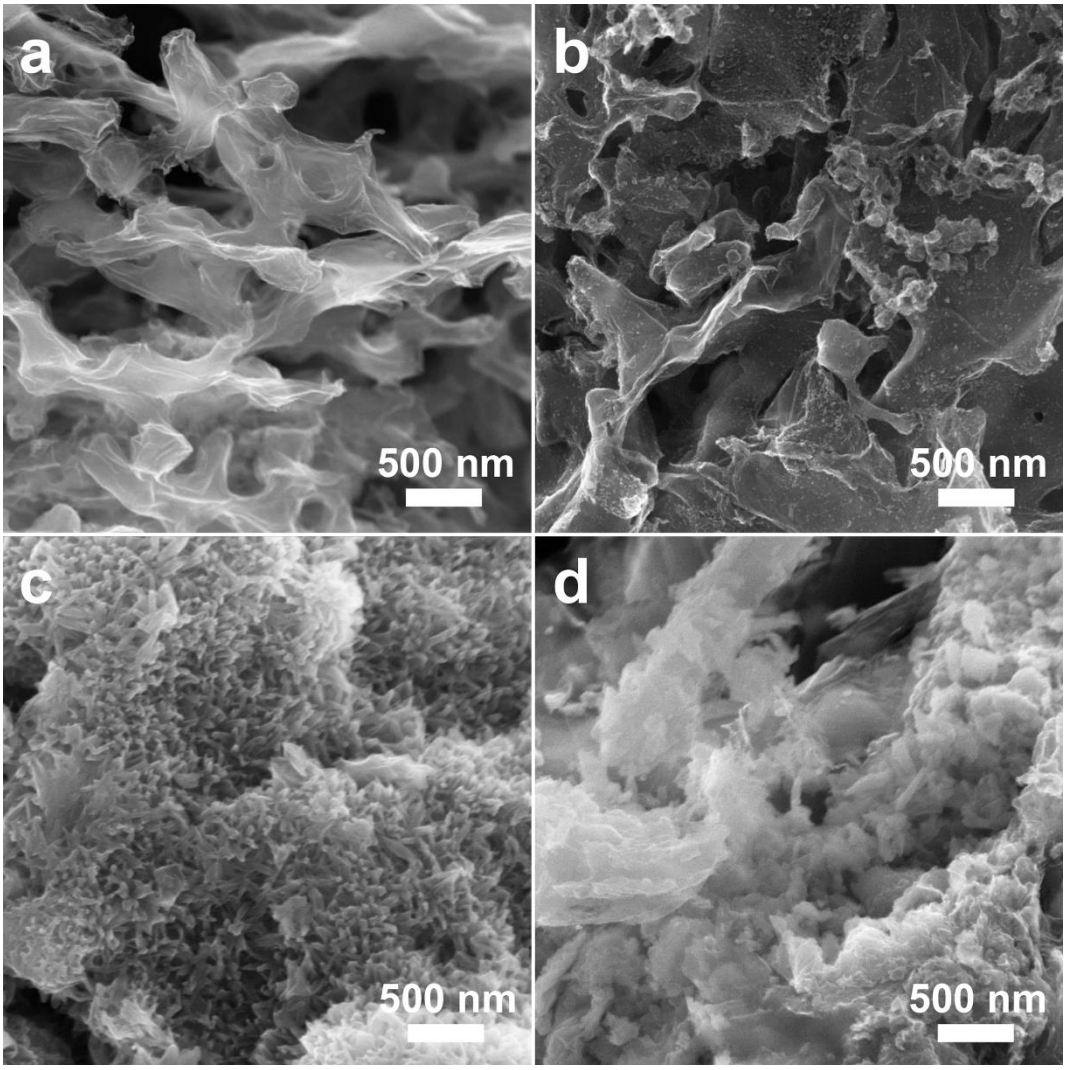

Figure S7. SEM images for samples prepared at different annealing durations (a-b) or ramp rates (c-d). (a) Fe_3C/NC-0.5H, (b) Fe_3C/NC-4H, (c) Fe_3C/NC-1R, (d) Fe_3C/NC-5R.

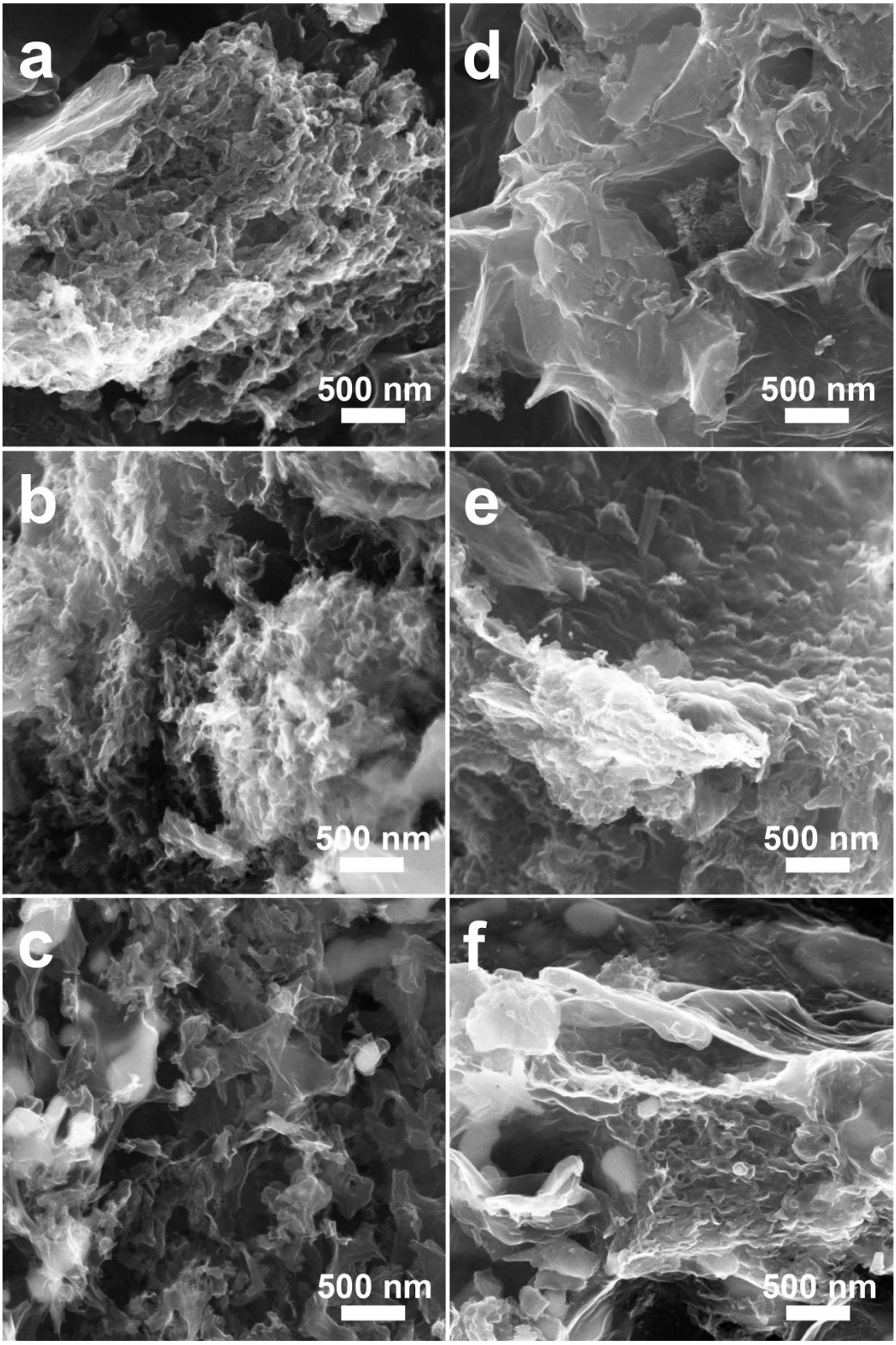

Figure S8. SEM images for samples prepared using different dosages of reactants. (a) Fe_3C/NC-0.5Fe, (b) Fe_3C/NC-2Fe, (c) Fe_3C/NC-0.5C, (d) Fe_3C/NC-2C, (e) Fe_3C/NC-0.5NTA, (f) Fe_3C/NC-2NTA.

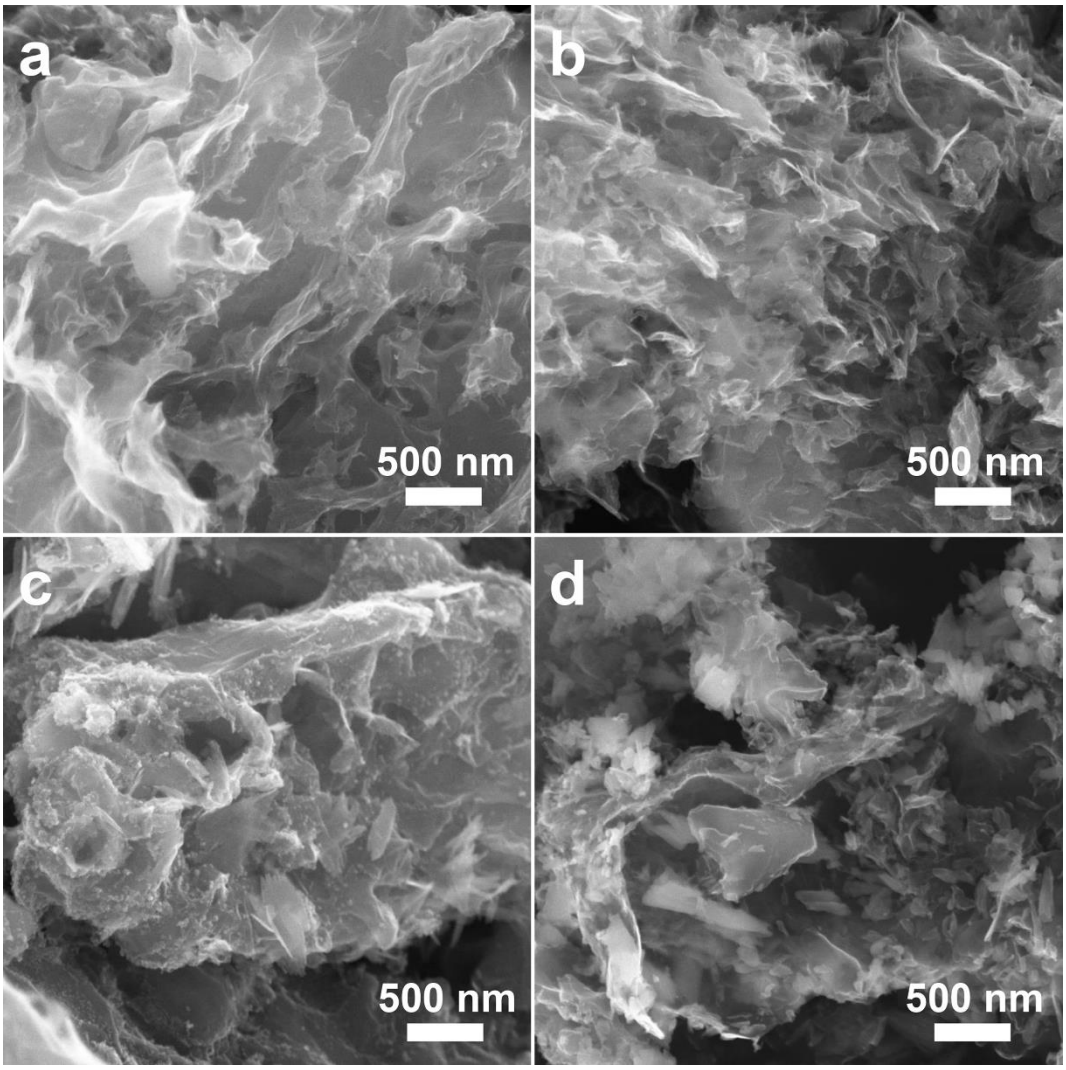

Figure S9. SEM images for catalysts prepared at different solvothermal temperatures (a-b) and durations (c-d). (a) Fe_3C/NC-140, (b) Fe_3C/NC-220, (c) Fe_3C/NC-3h, (d) Fe_3C/NC-9h.

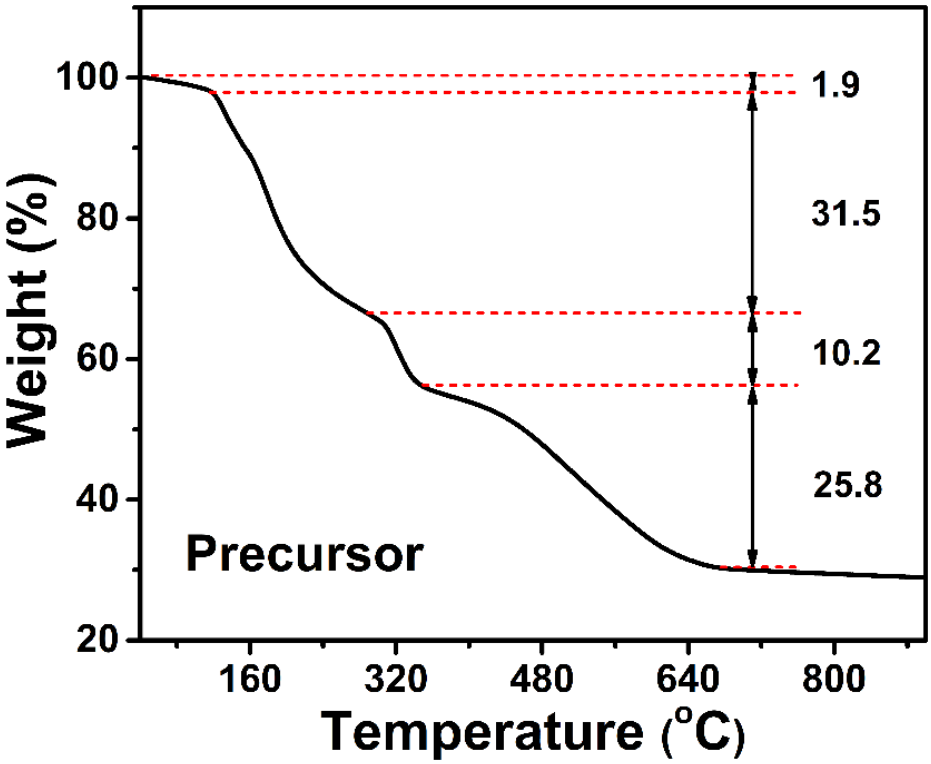

Figure S10. TG curves of the Fe-NTA complex under Ar with a ramp rate of 10 °C min^{-1}.

Table S2. Origin of weight losses in TG curves of the Fe-NTA complex under Ar.

Temperature (°C)	Origin of weight losses
<175	Evaporation of surface adsorbed moistures
175-350	Partial decomposition of NTA
350-700	Graphitization of the carbon species and formation of Fe and Fe_3C

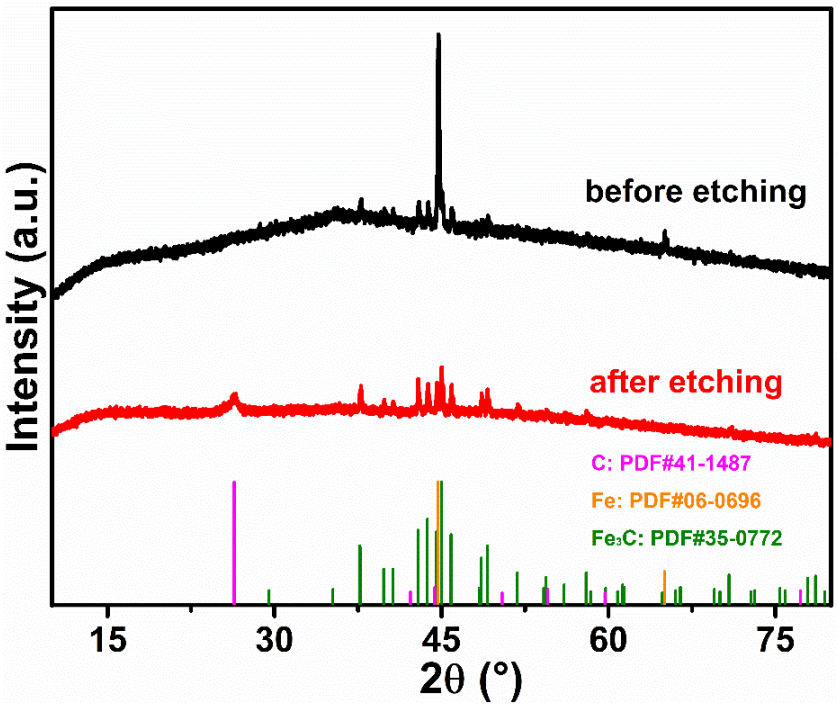

Figure S11. XRD patterns of the annealed sample before (black) and after (red) etching in 2 M HCl for 12 h. The metallic species of Fe were removed by etching.

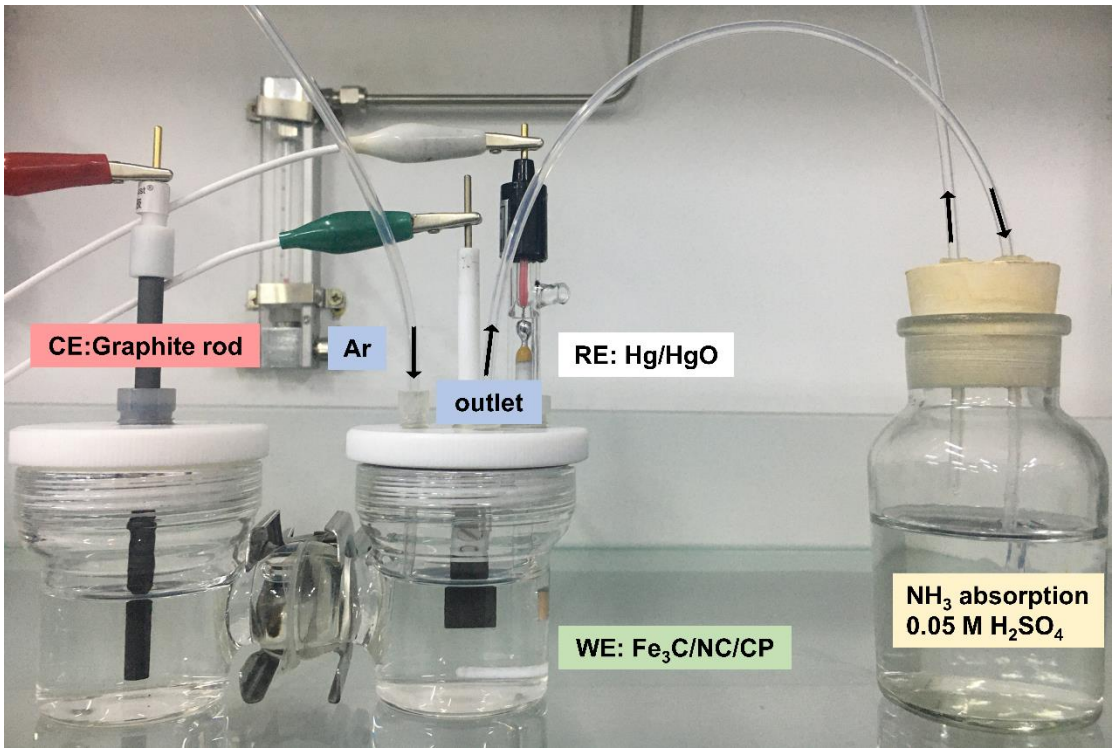

Figure S12. Photograph of the reactor for NO_3RR with a gas absorption device connected with the outlet to capture and collect the lost NH_3 in the gas phase. 0.05 M H_2SO_4 aqueous solution was used to trap the escaped NH_3.

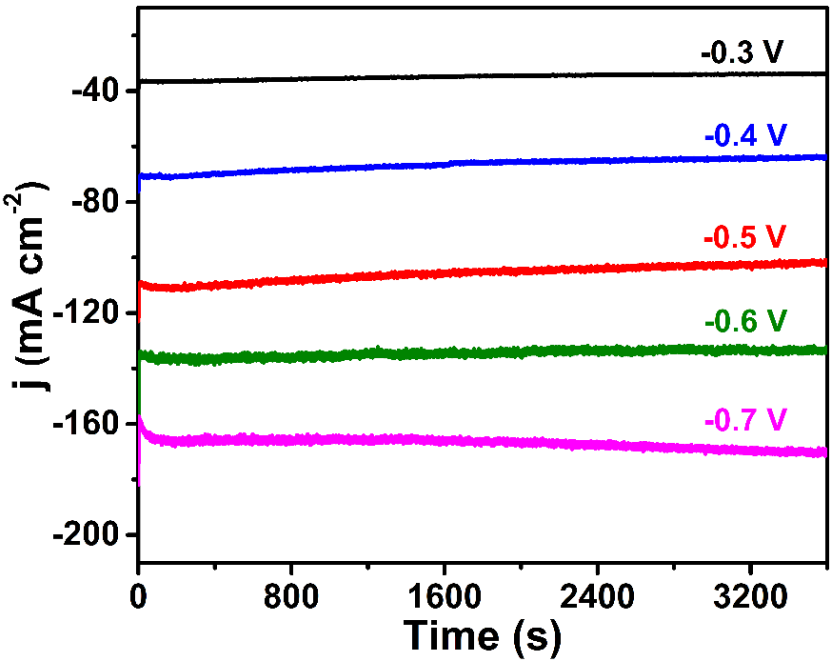

Figure S13. Chronoamperometric results for Fe_3C/NC at different potentials.

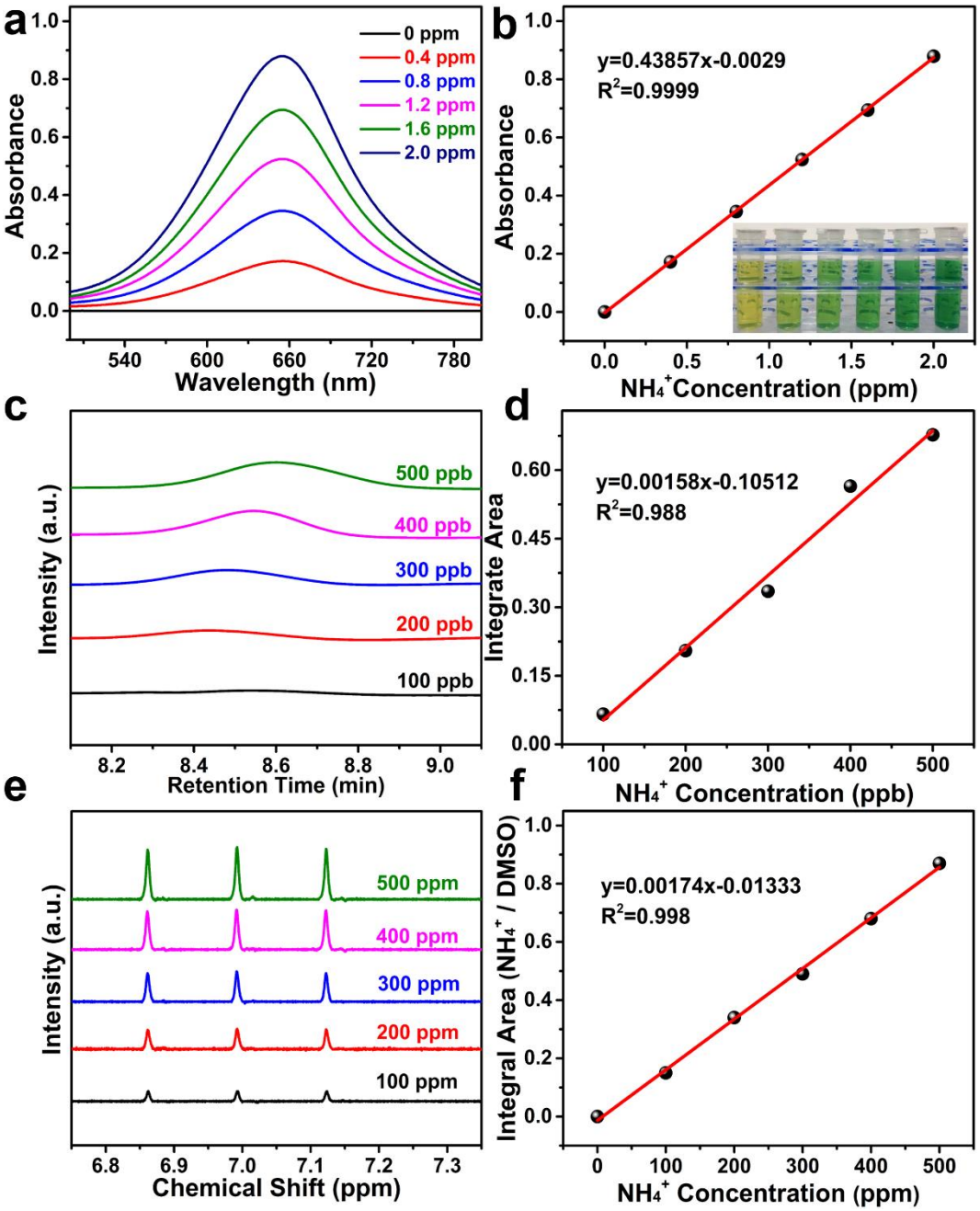

Figure S14. UV-vis absorption spectra of NH_4^+ standard solutions stained with indophenol blue (a), the corresponding calibration curves (b) and the photograph of the colorimetric assays (inset in b). IC spectra of NH_4^+ standard solutions (c) and the corresponding calibration curves (d). ^1H NMR spectra (400 MHz) of NH_4^+ standard solutions with pH values adjusted to 3 (e) and the corresponding calibration curves (f).

Table S3. Yield, faradaic efficiency (FE) and selectivity of NH_3 at different potentials for Fe_3C/NC determined by three methods including the indophenol blue method (UV), the ion chromatography (IC) and ^{1}H-nuclear magnetic resonance (NMR) spectra.

Potential (V vs. RHE)	Yield (mmol· mg^{-1}· h^{-1})			FE (%)			Selectivity (%)		
	UV	IC	NMR	UV	IC	NMR	UV	IC	NMR
-0.3	0.37	0.39	0.35	91.2	96.1	85.8	78.1	84.5	73.5
-0.4	0.74	0.75	0.72	95.1	96.8	92.7	78.5	79.8	76.6
-0.5	1.19	1.16	1.16	96.7	94.0	94.1	79.0	76.8	76.9
-0.6	1.44	1.34	1.36	91.7	85.4	86.9	86.5	80.6	82.0
-0.7	1.77	1.80	1.63	90.8	92.5	83.9	86.1	87.7	79.5

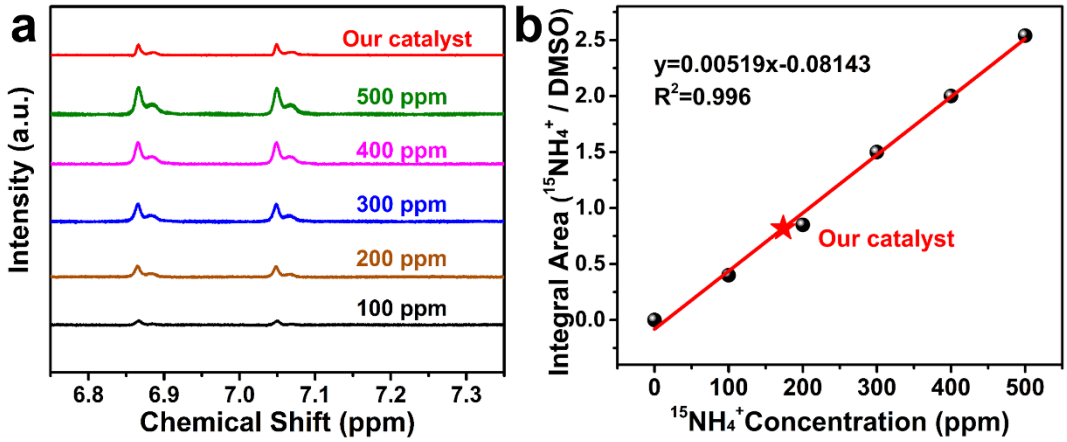

Figure S15. Quantification of the produced ammonia using $K^{15}NO_3$ as the feeding nitrate. ^{1}H-NMR spectra (a) and the corresponding calibration curve (b) of the standard solutions of $^{15}NH_4Cl$. For comparison, the ^{1}H-NMR spectrum and the concentration of $^{15}NH_4^+$ of our work were also included in (a) and (b), respectively. The electrolysis was performed at -0.5 V for 1 h in aqueous solutions containing 75 mM $K^{15}NO_3$ and 1 M KOH with Fe_3C/NC as the catalyst.

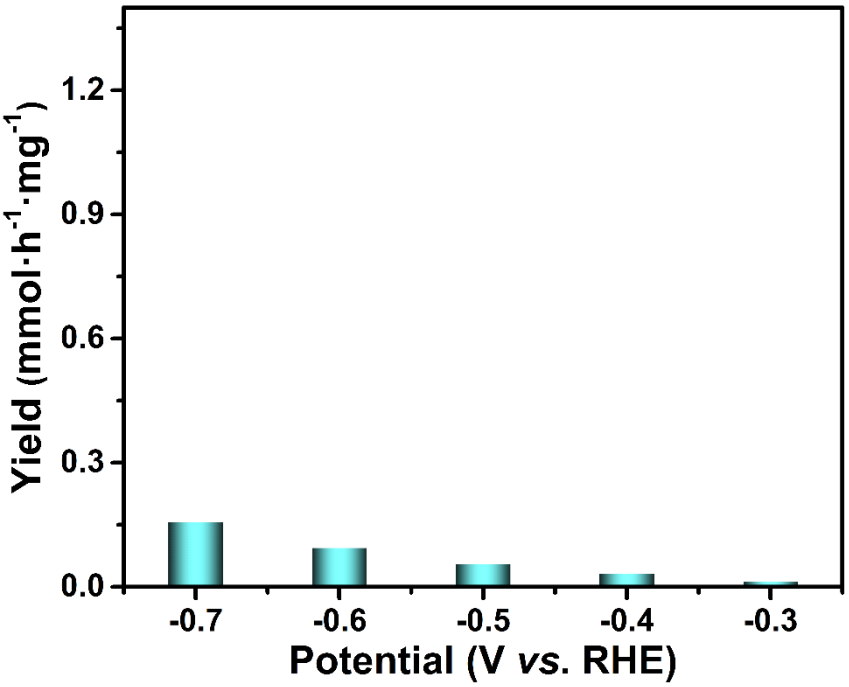

Figure S16. Yield of NH_3 for NC after electrolysis in in aqueous solutions containing 1 M KOH and 75 mM KNO_3 for 1 h at different potentials.

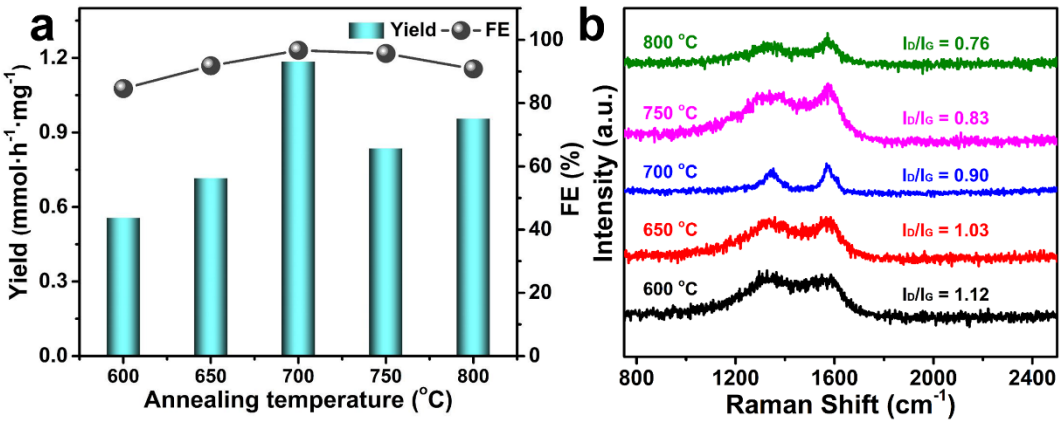

Figure S17. Yield and FE of NH_3 (a) and Raman spectra (b) for Fe_3C/NC-600, Fe_3C/NC-650, Fe_3C/NC, Fe_3C/NC-750 and Fe_3C/NC-800. Electrolysis was conducted at -0.5 V for 1 h in aqueous solutions contsianing 1 m KOH and 75 mM KNO_3.

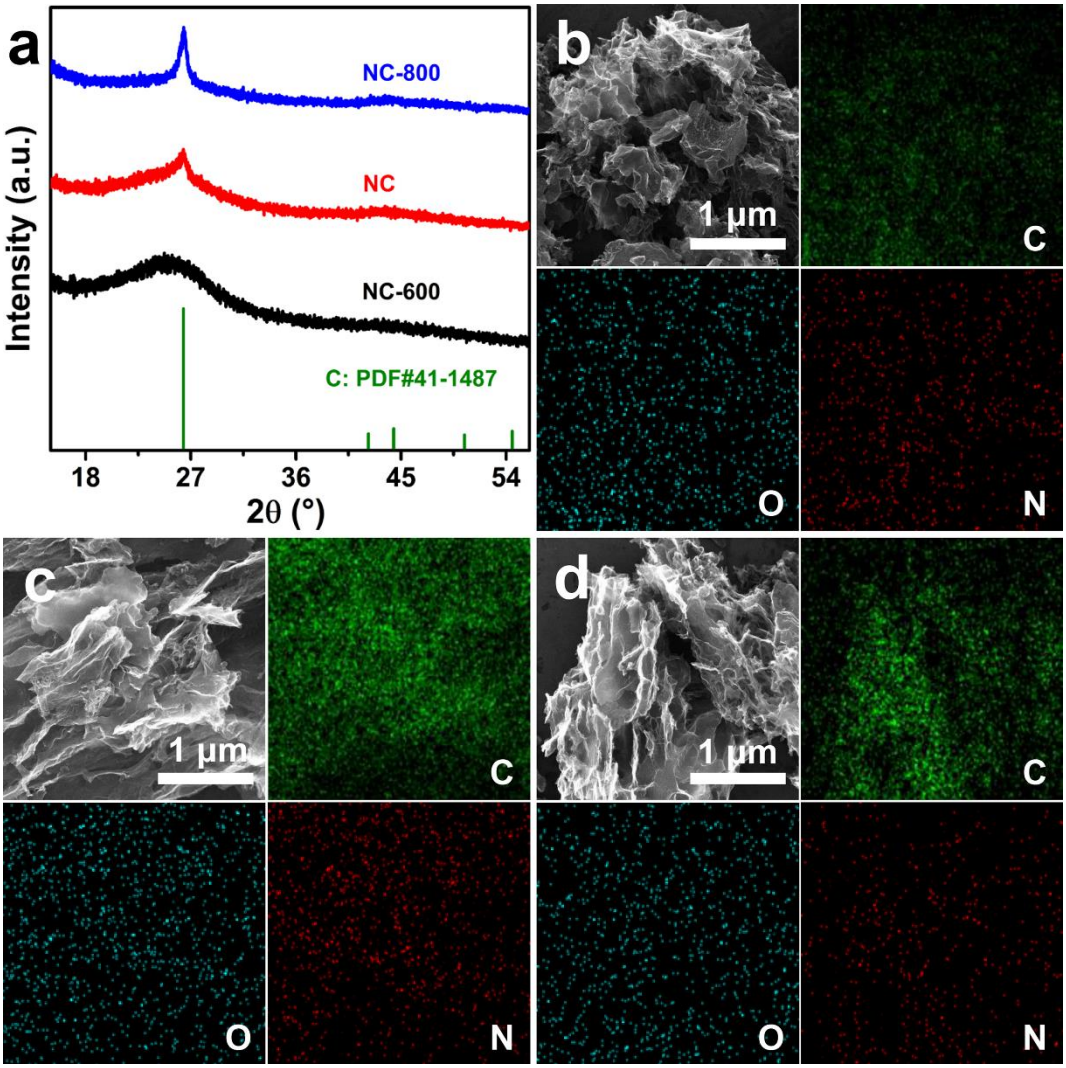

Figure S18. Structural characterizations for carbon supports prepared at different annealing temperatures. XRD patterns (a), SEM and EDS elemental mapping images (b-d) for NC-600 (b), NC (c) and NC-800 (d).

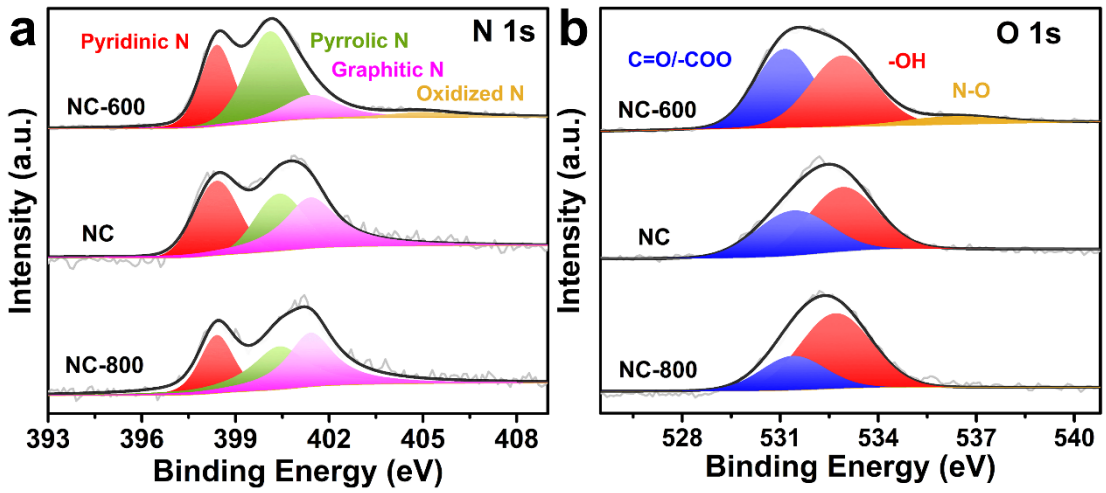

Figure S19. N 1s (a) and O 1s (b) XPS for NC-600, NC and NC-800.

Table S4. Contents of N, O and C in NC-600, NC and NC-800 from XPS analyses.

Sample	C (at%)	N (at%)	O (at%)	N/O
NC-600	80.54	10.85	8.61	1.26
NC	89.07	5.36	5.57	0.96
NC-800	91.52	3.75	4.73	0.79

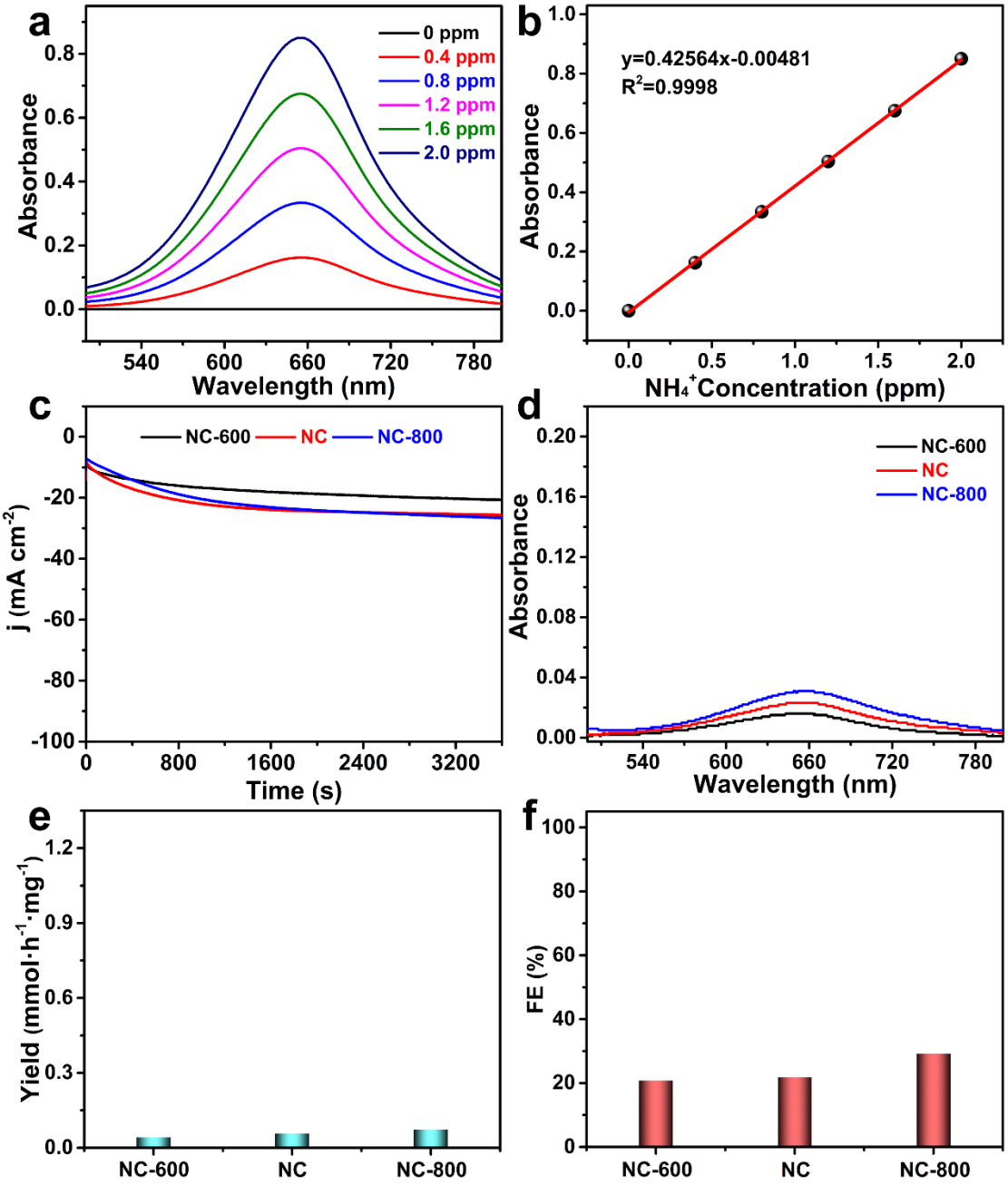

Figure S20. NO_3RR performances for carbon supports prepared at different annealing temperatures. UV-absorption spectra (a) and the calibration curve (b) of standard NH_4Cl aqueous solutions. Chronoamperometric responses (c), UV-vis absorption spectra (d) and yield (e) and FE (f) of NH_3 for NC-600, NC and NC-800 (d) after electrolysis at -0.5 V for 1 h in aqueous solutions of 1 M KOH and 75 mM KNO_3.

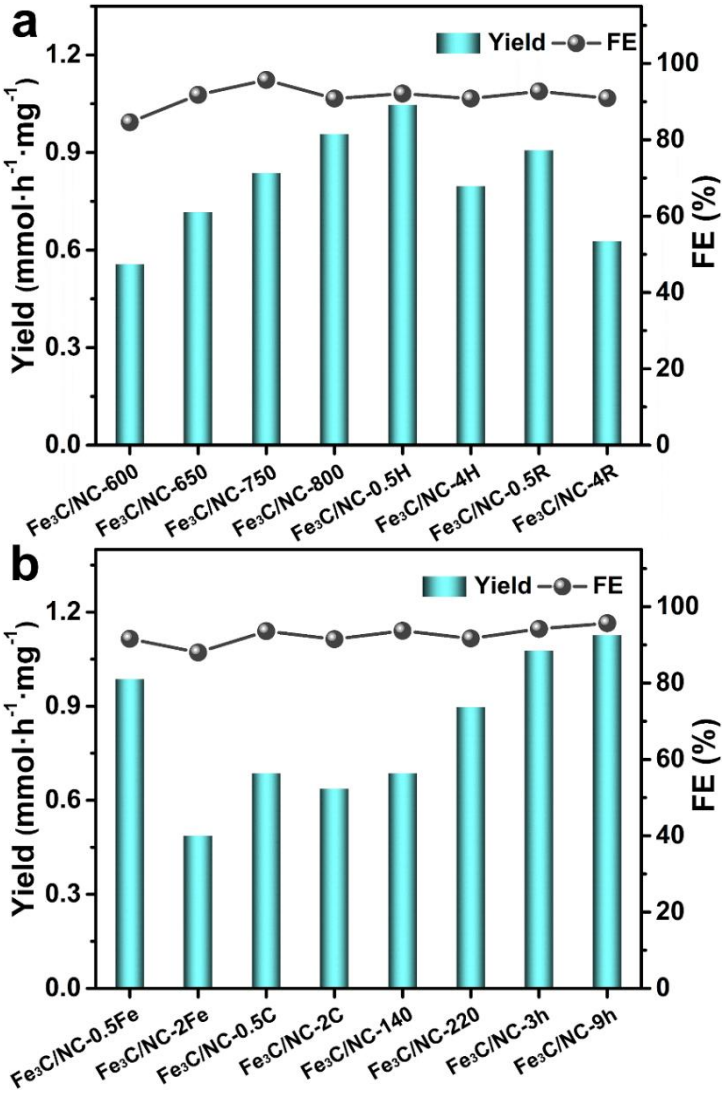

Figure S21. NO_3RR performances for samples prepared under different annealing (a) and solvothermal (b) conditions.

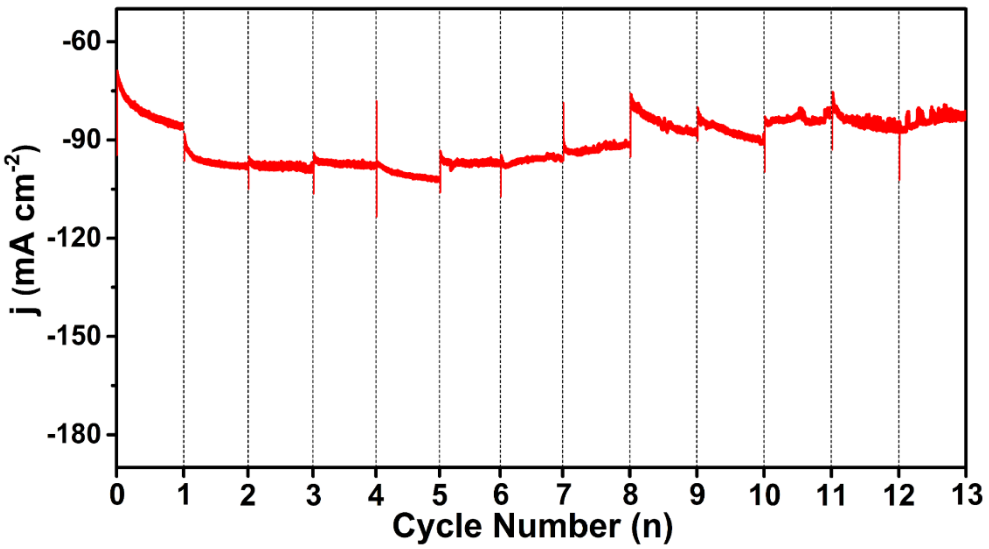

Figure S22. Chronoamperometric responses during the recycling test for Fe_3C/NC at -0.5 V vs. RHE in an aqueous solution containing 1 M KOH and 75 mM KNO_3

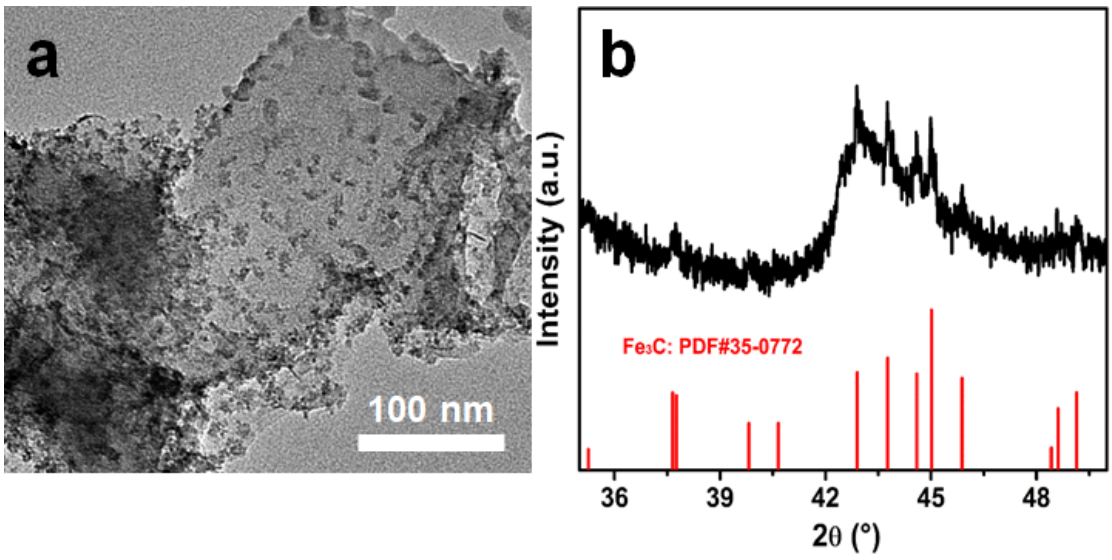

Figure S23. TEM images (a) and XRD patterns (b) for Fe_3C/NC after recycling for 13 runs.

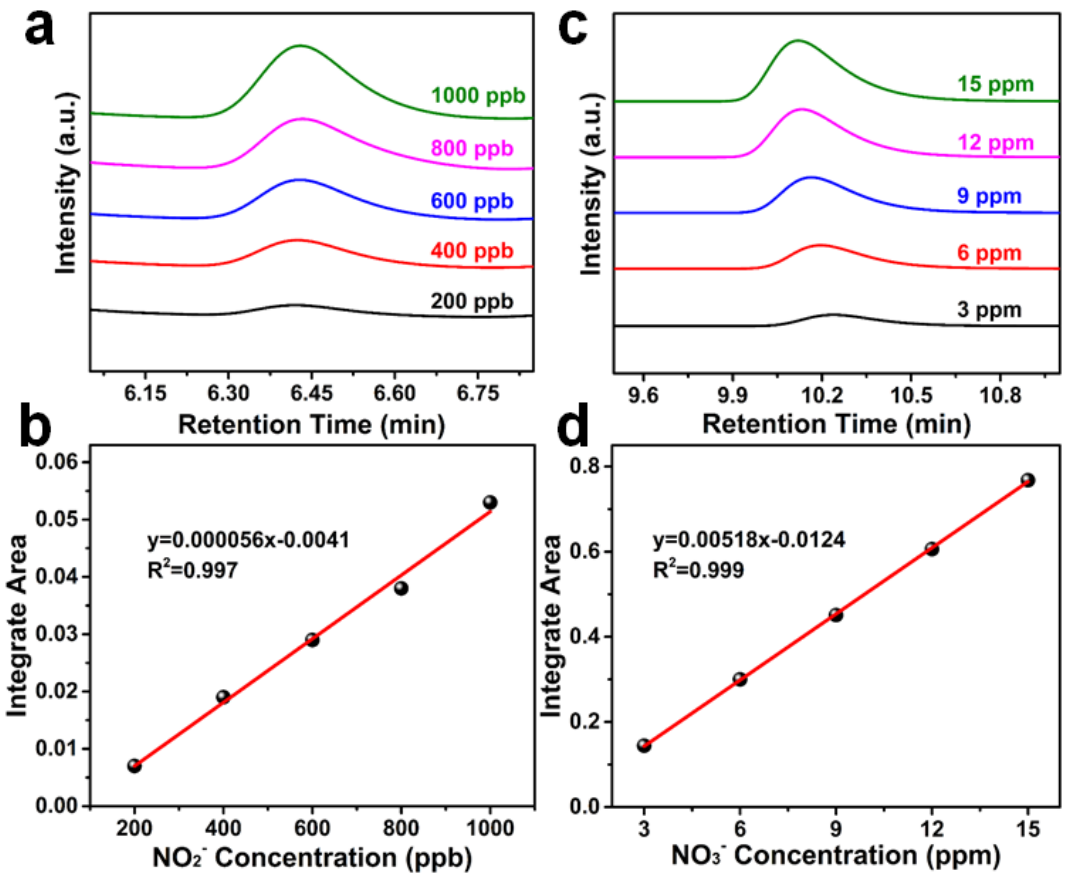

Figure S24. IC spectra (a, c) and the corresponding calibration curves (b, d) of NO_2^- (a-b) and NO_3^- (c-d) standard solutions.

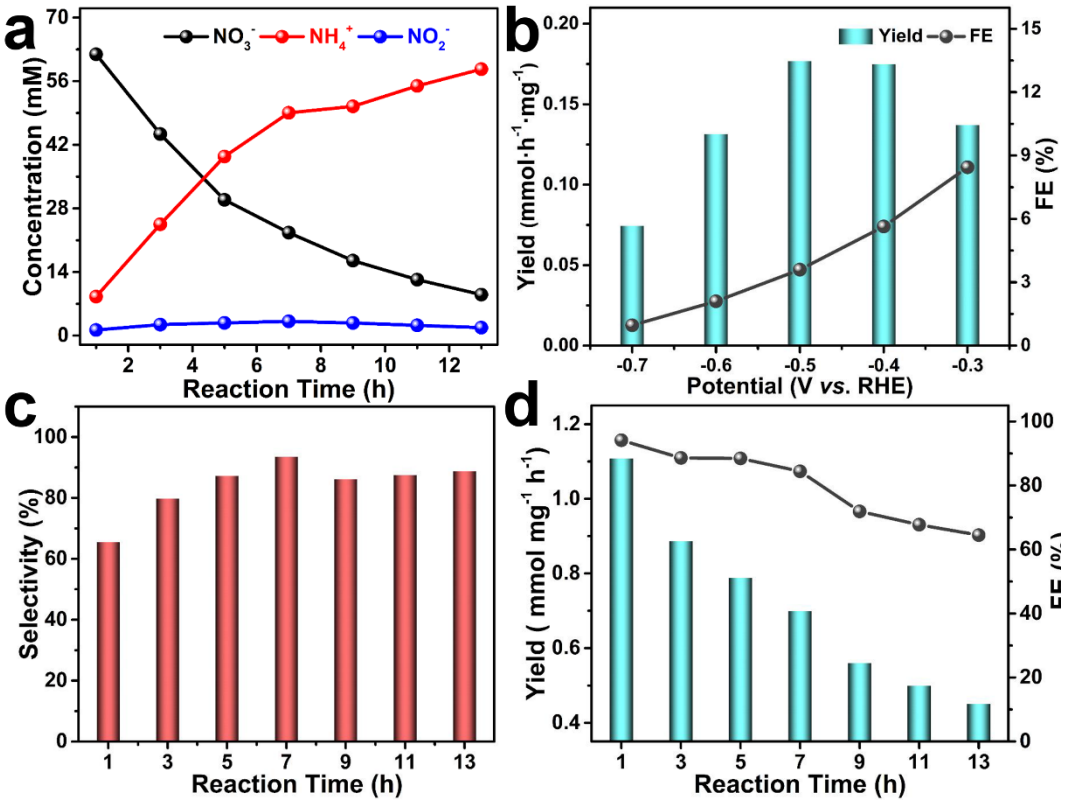

Figure S25. Time-dependent concentrations of NO_3^-, NO_2^- and NH_4^+ (a) and the corresponding selectivity (c), yield and faradaic efficiency (d) of NH_4^+ during the continuous long-term electrolysis for 13 h at -0.5 V. Potential-dependent yield and faradaic efficiency of NO_2^- after chronoamperometric electrolysis for 1 h in 1 M KOH and 75 mM KNO_3 (b).

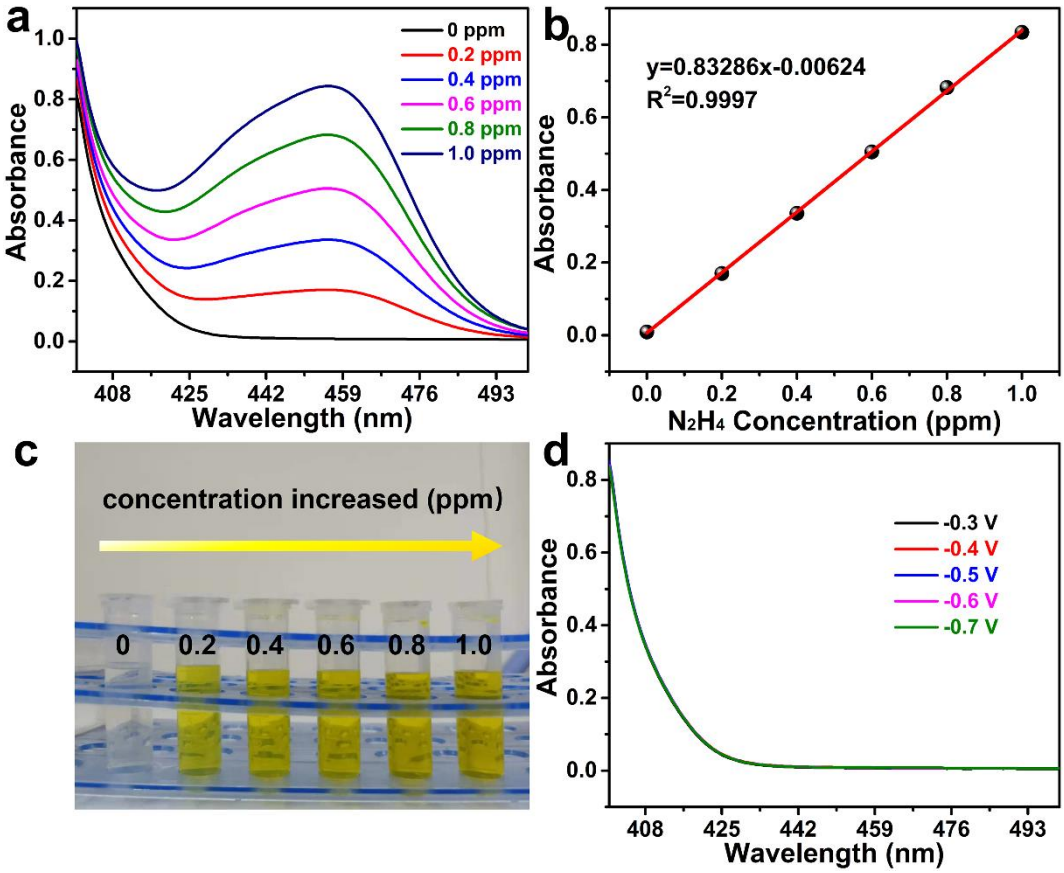

Figure S26. Determination of the possible by-product of N_2H_4 using the Watt-Chrisp method. (a) UV-vis absorption spectra, (b) the calibration curve and (c) the photograph of N_2H_4 standard solutions after color development. (d) UV-vis absorption spectra of the catholytes with the addition of the color reagent after electrolysis in 1 M KOH and 75 mM KNO_3 for 1 h at different potentials.

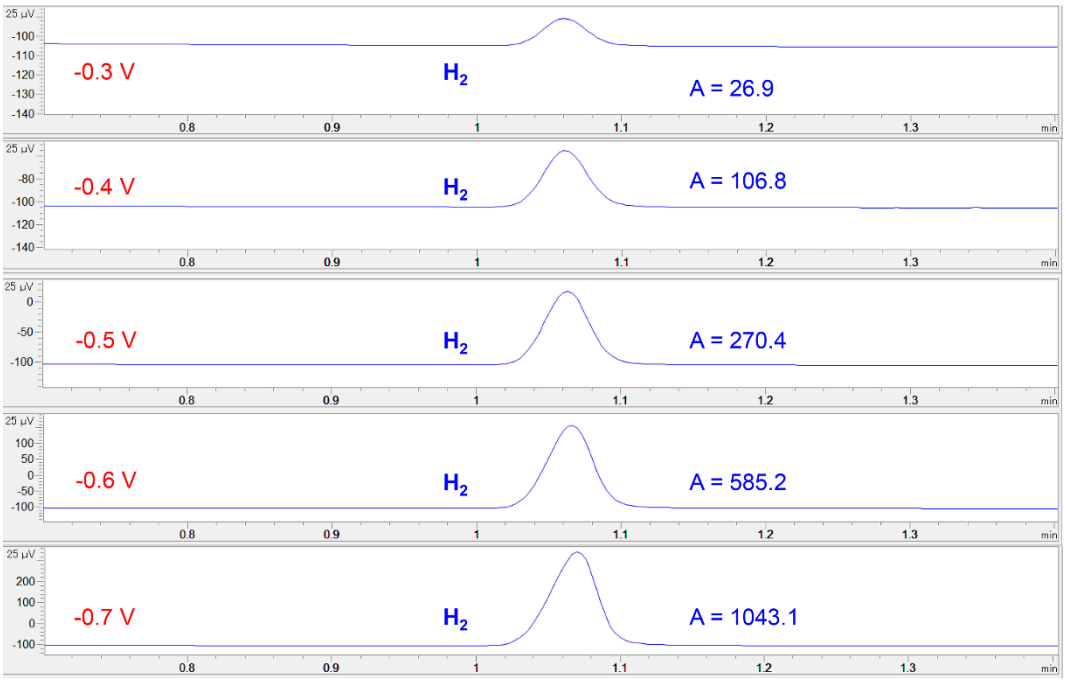

Figure S27. Gas chromatography (GC, Agilent Technologies, 7890B) spectra of the products after electrolysis at different potentials in 1 M KOH aqueous solutions without KNO_3 using Fe_3C/NC as the catalyst. The peaks appeared at about 1.06 min can be assigned to H_2, which was probably another by-product of NO_3RR. The corresponding peak areas (A) increased as the potentials became more negative, indicating the increase of the amount of generated H_2.

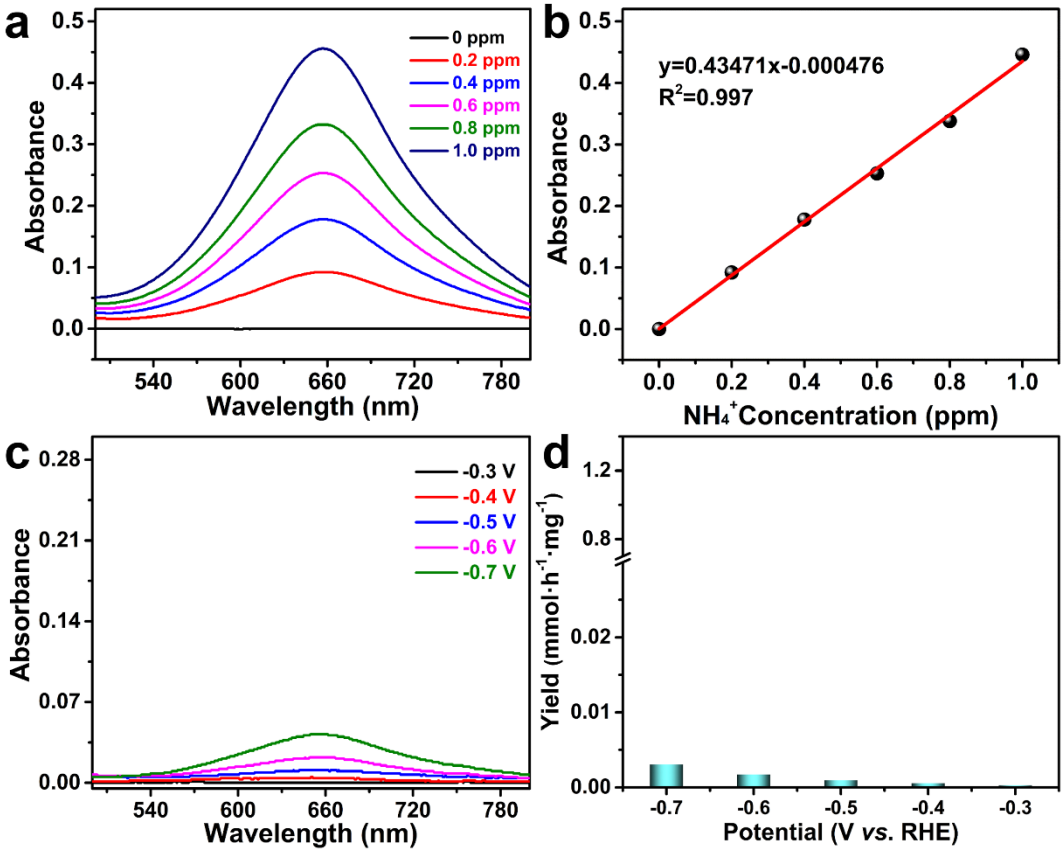

Figure S28. Determination of the possible escaped NH_3 in the gas phase. UV-vis absorption spectra (a) and the corresponding calibration curve (b) of the standard solutions of NH_4Cl stained with indophenol blue. UV-vis absorption spectra (c) and the calculated yields (d) of the trapped NH_4^+ in the 0.05 M H_2SO_4 solution connected with the outlet of the reactor.

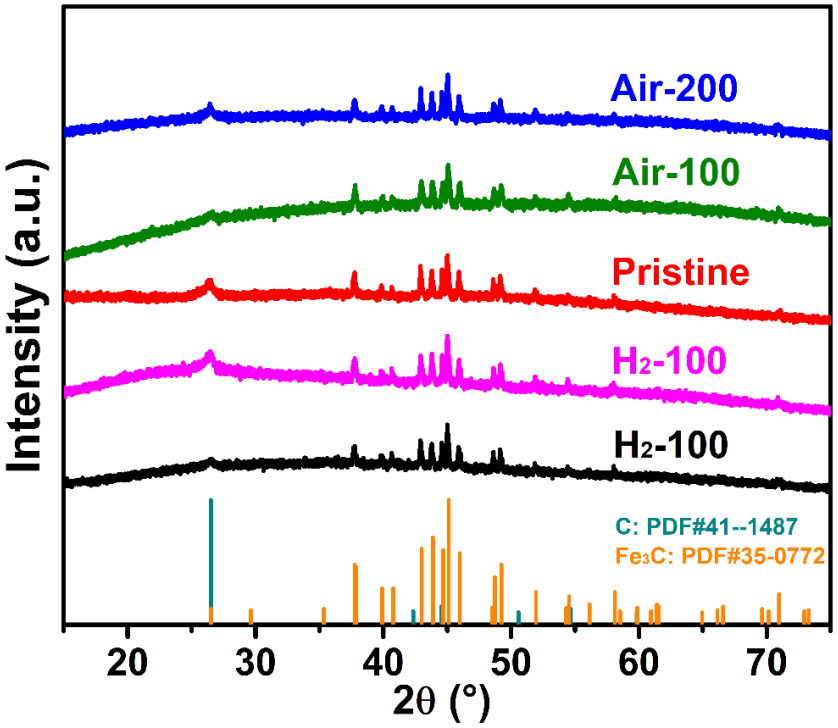

Figure S29. XRD patterns for Air-200, Air-100, H_2-100, H_2-300 and the pristine sample of Fe_3C/NC.

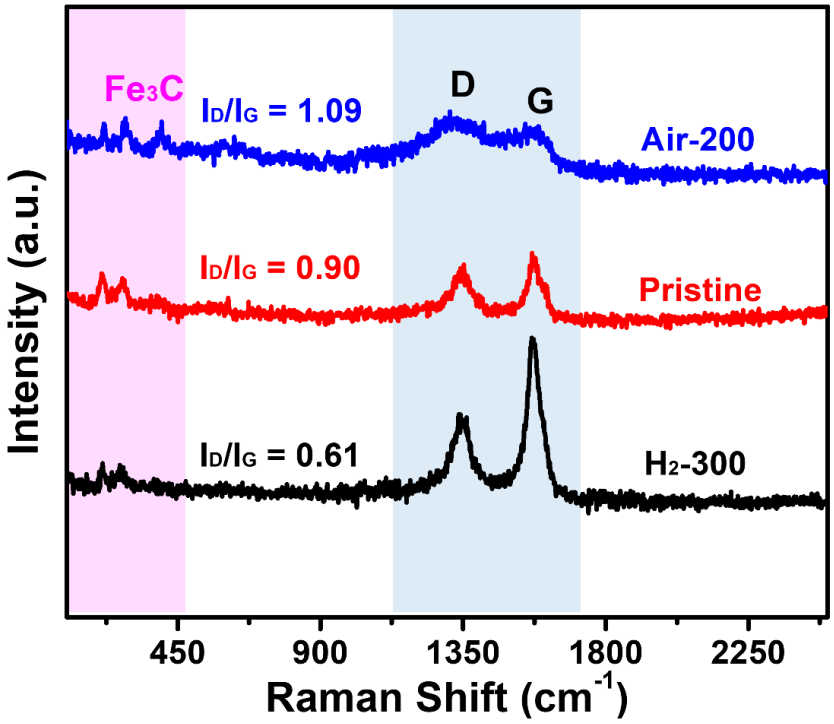

Figure S30. Raman spectra of H_2-300, Air-200 and the pristine sample of Fe_3C/NC.

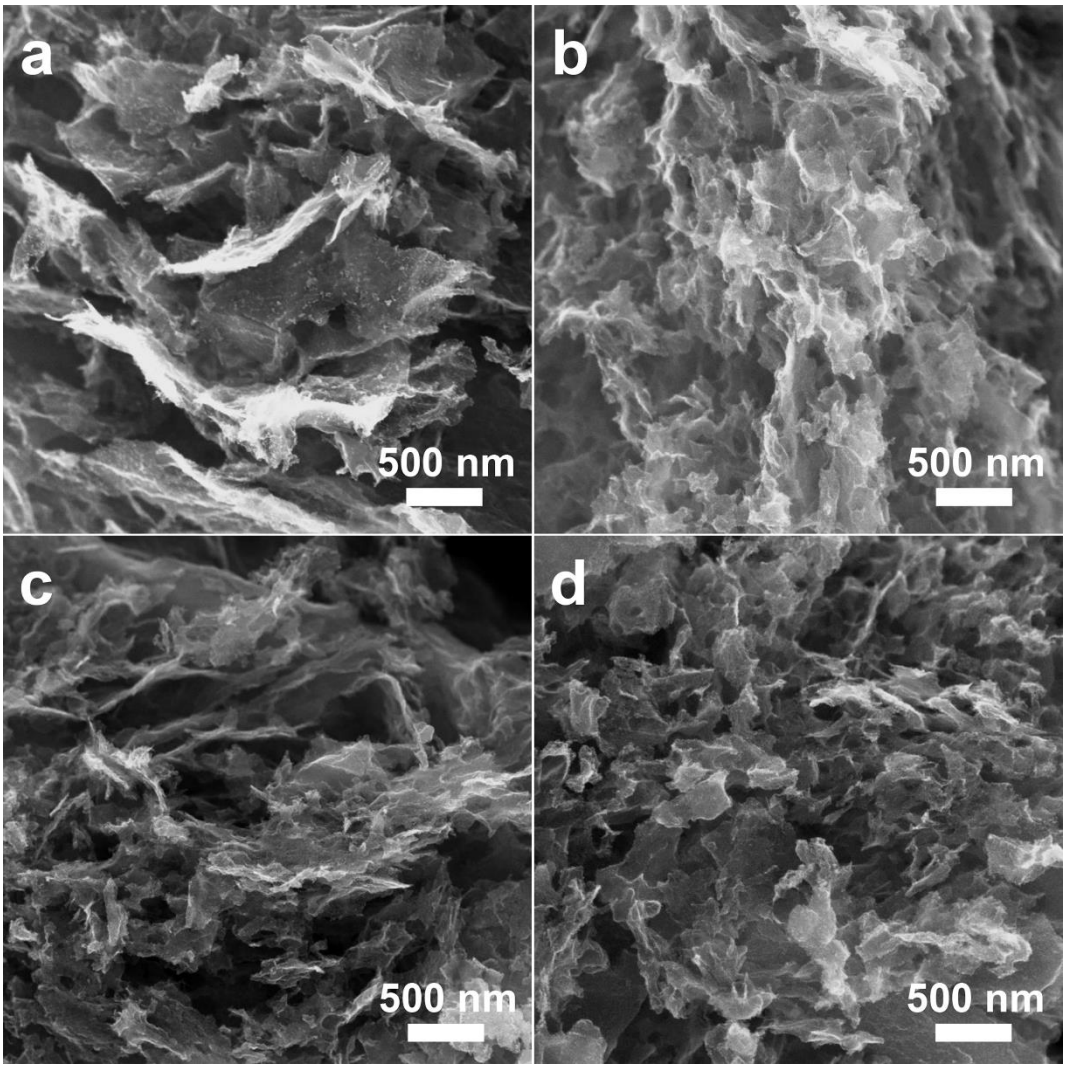

Figure S31. SEM images for Air-200 (a), Air-100 (b), H_2-100 (c) and H_2-300 (d).

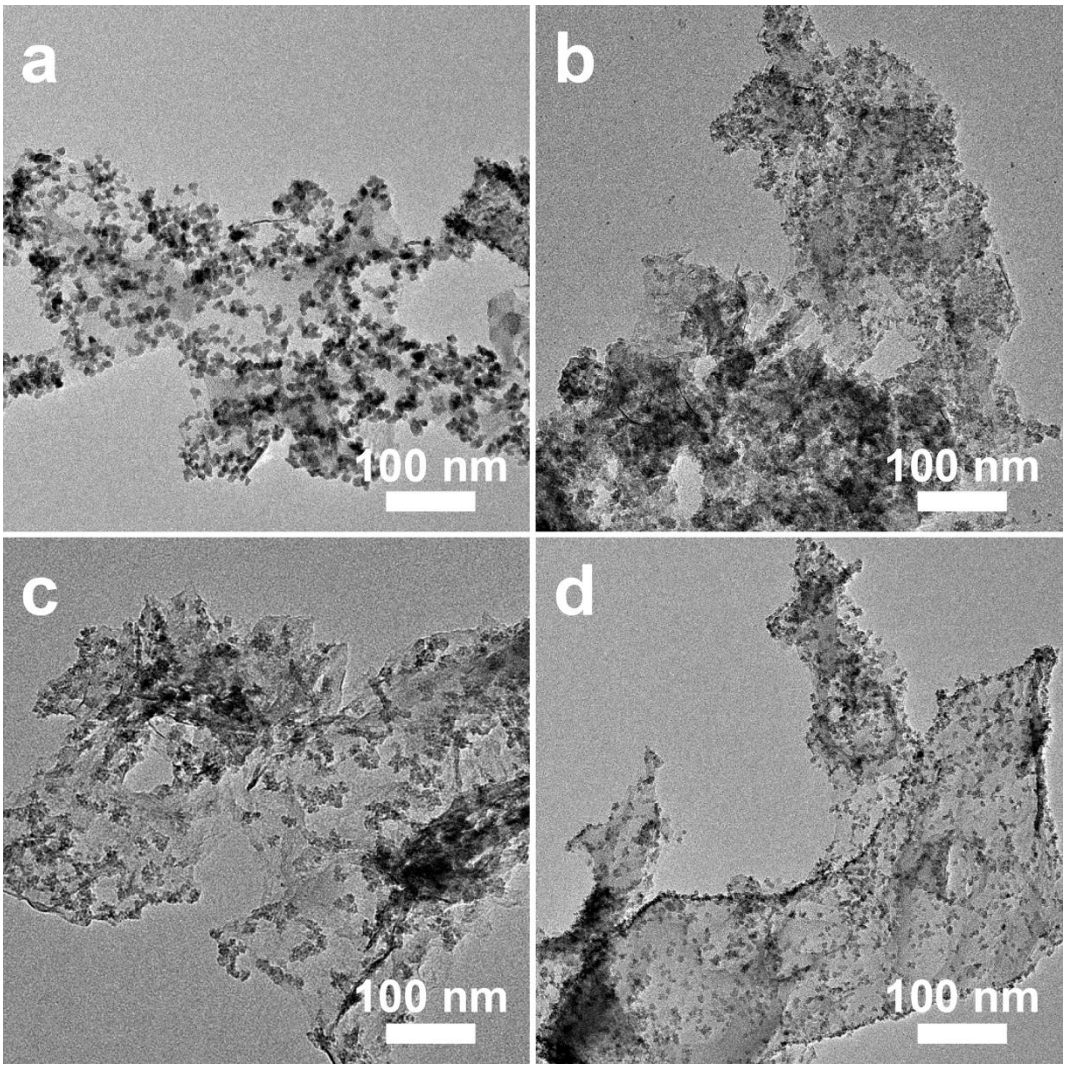

Figure S32. TEM images for Air-200 (a), Air-100 (b), H_2-100 (c) and H_2-300 (d).

Table S5. Contents of Fe, C, N, H and O elements in the as-synthesized samples

Sample	ICP-MS	EA			Calculated
	Fe (wt%)	C (wt%)	N (wt%)	H (wt%)	O (wt%)
Air-200	35.6	45.4	4.9	1.0	13.1
Air-100	33.8	47.9	4.8	1.5	12
Pristine	33.6	46.9	4.8	1.3	13.6
H_2-100	33.2	45.1	4.5	1.4	15.8
H_2-300	33.4	47.0	4.8	1.2	13.6

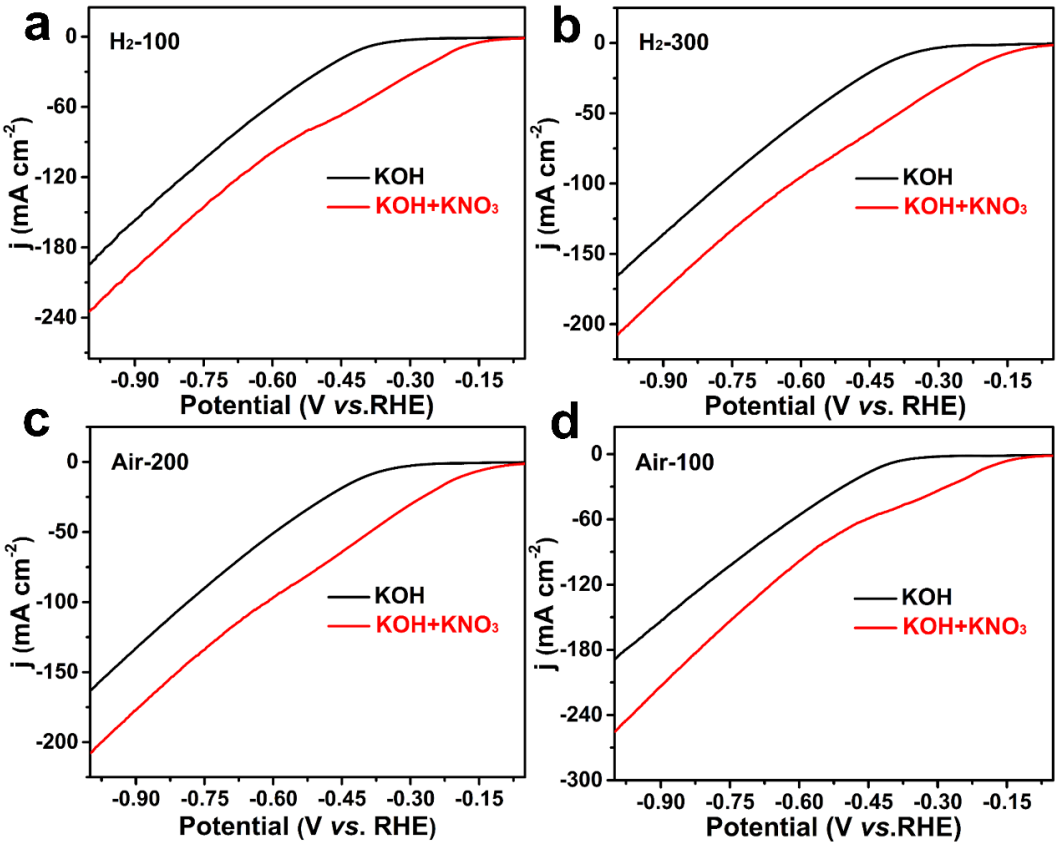

Figure S33. LSV curves for H_2-300 (a), H_2-100 (b), Air-100 (c) and Air-200 (d) in 1 M KOH aqueous solutions with or without 75 mM KNO_3.

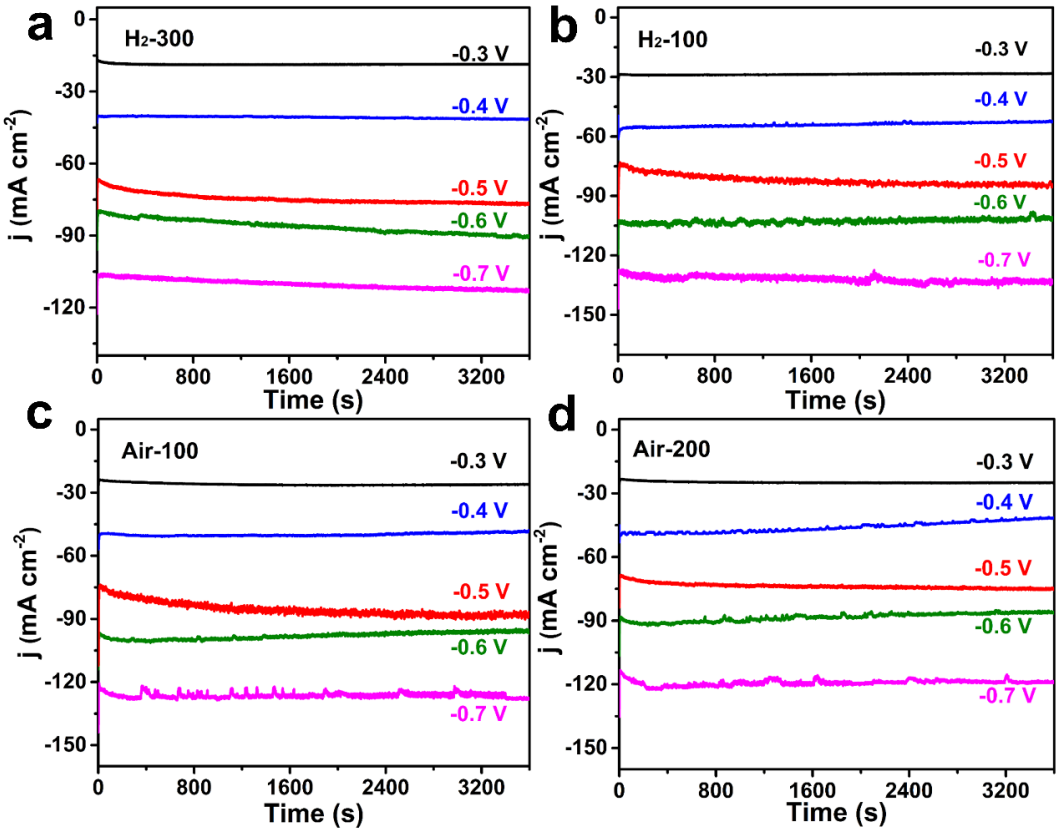

Figure S34. Chronoamperometric responses at different potentials for Air-200 (a), Air-100 (b), H_2-100 (c) and H_2-300 (d) in aqueous solutions containing 1 M KOH and 75 mM KNO_3.

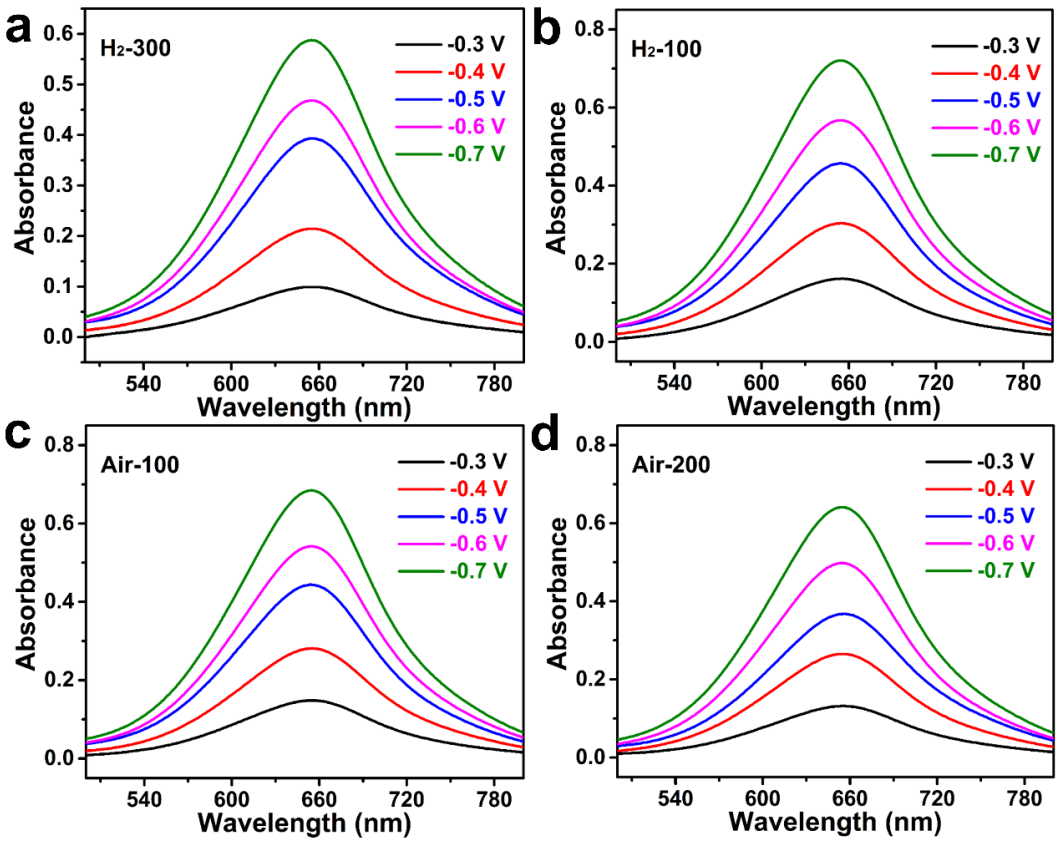

Figure S35. UV-vis absorbance spectra of the indophenol blue-stained catholytes after electrolysis at given potentials with Air-200 (a), Air-100 (b), H_2-100 (c) and H_2-300 (d) as the catalysts, respectively.

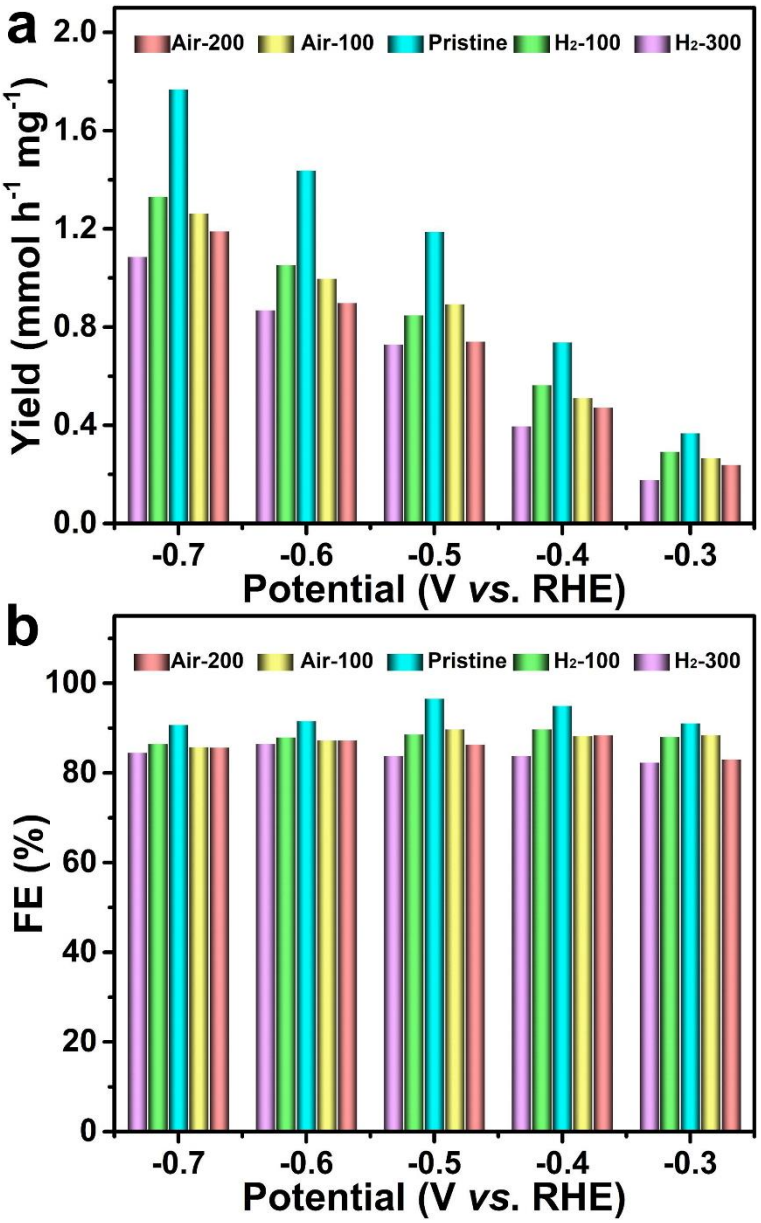

Figure S36. Yield (a) and FE (b) of NH_3 at different potentials for Air-200, Air-100, H_2-100 and H_2-300. For comparison, the data for the pristine sample of Fe_3C/NC was also included.

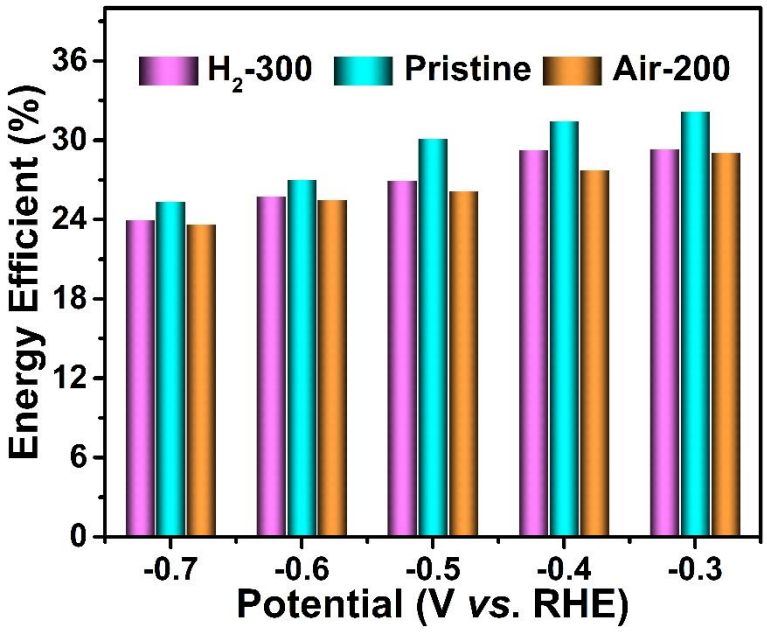

Figure S37. Potential-dependent energy efficiencies for nitrate reduction to ammonia over Air-200, H_2-300 and the pristine sample of Fe_3C/NC.

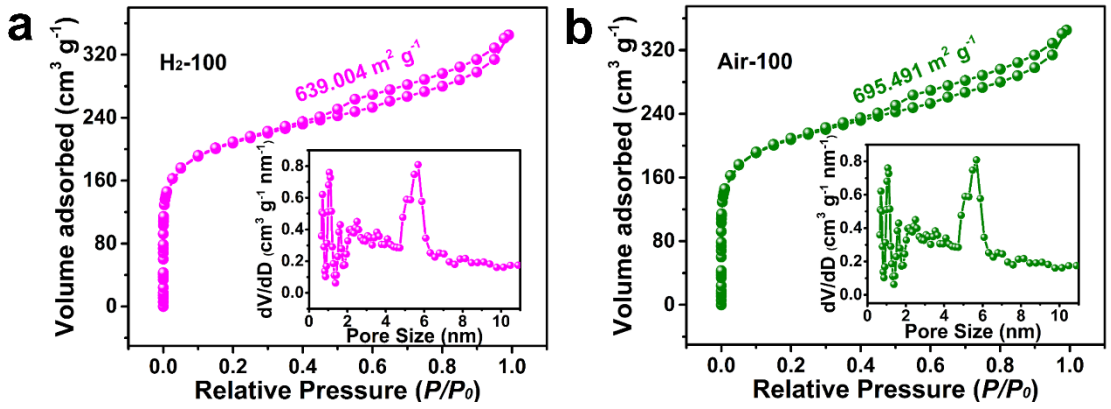

Figure S38. N_2 adsorption-desorption isotherms for Air-100 (a) and H_2-100 (b) and the corresponding pore size distributions (insets).

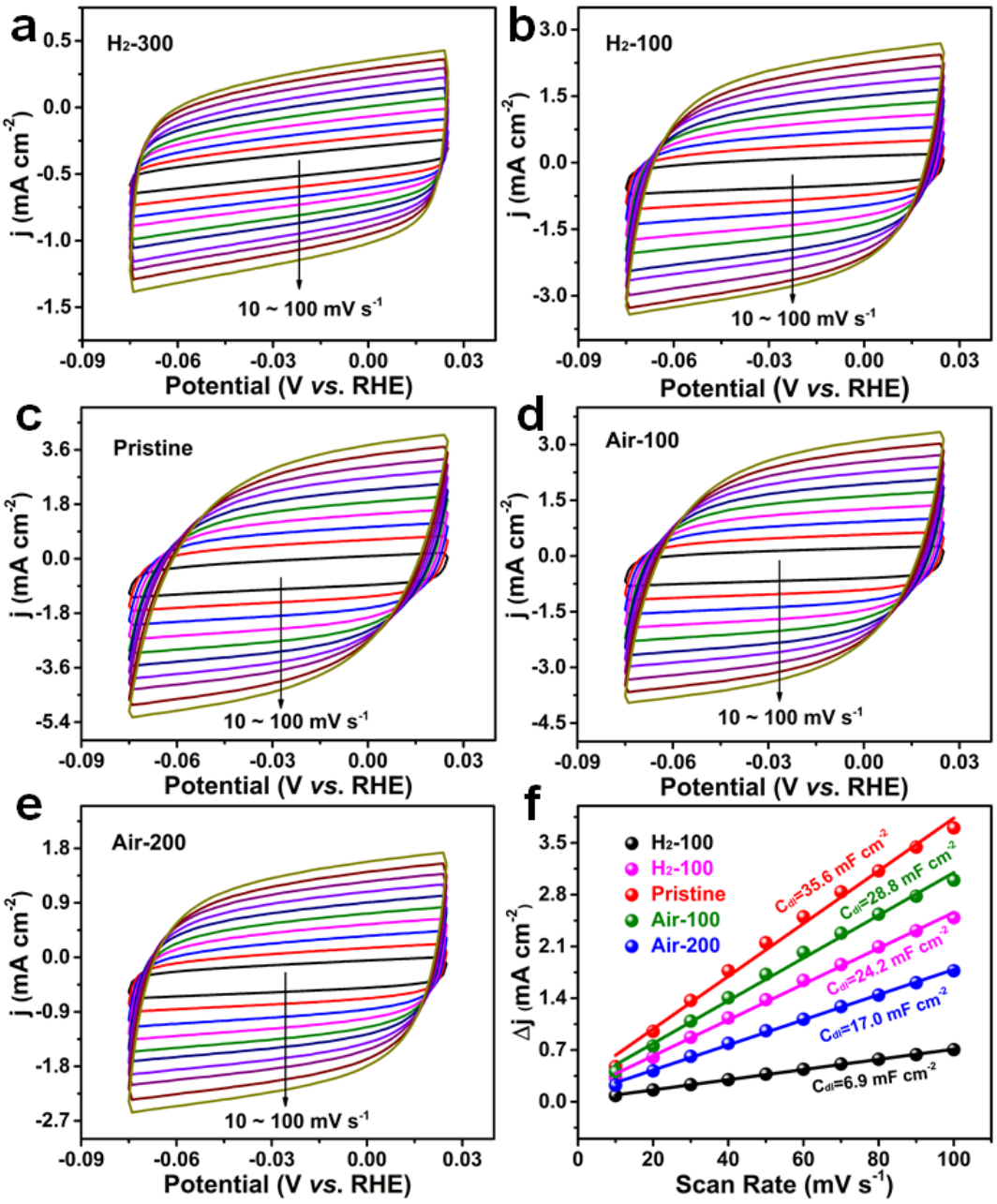

Figure S39. Cyclic voltammertry curves at scan rates from 10 to 100 mV s^{-1} for Air-200 (a), Air-100 (b), pristine sample of Fe_3C/NC (c), H_2-100 (d) and H_2-300 (e) and the derived double layer capacitances (C_{dl}, f).

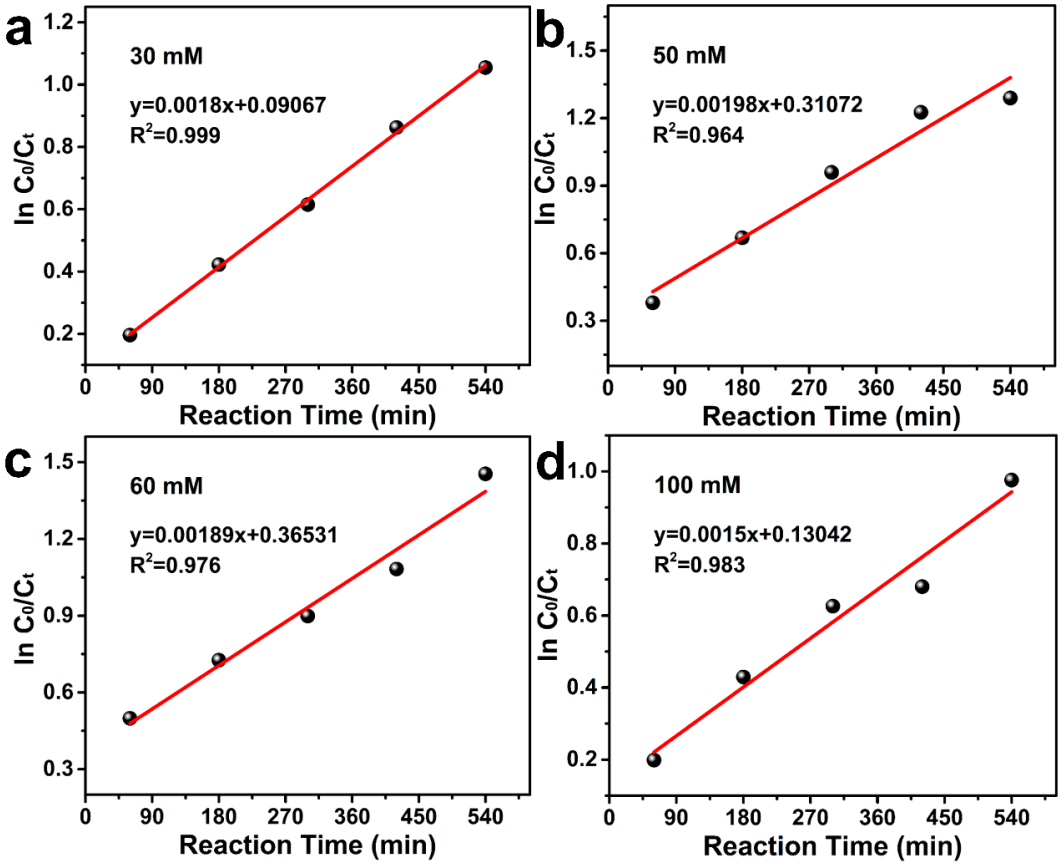

Figure S40. Linear fitting plots of $\ln C_0/C_t$ vs. reaction time t based on the pseudo first order kinetic equation for H_2-300 with different initial nitrate concentrations in the electrolytes at -0.5 V vs. RHE. (a) 30 mM, (b) 50 mM, (c) 60 mM, (d) 100 mM.

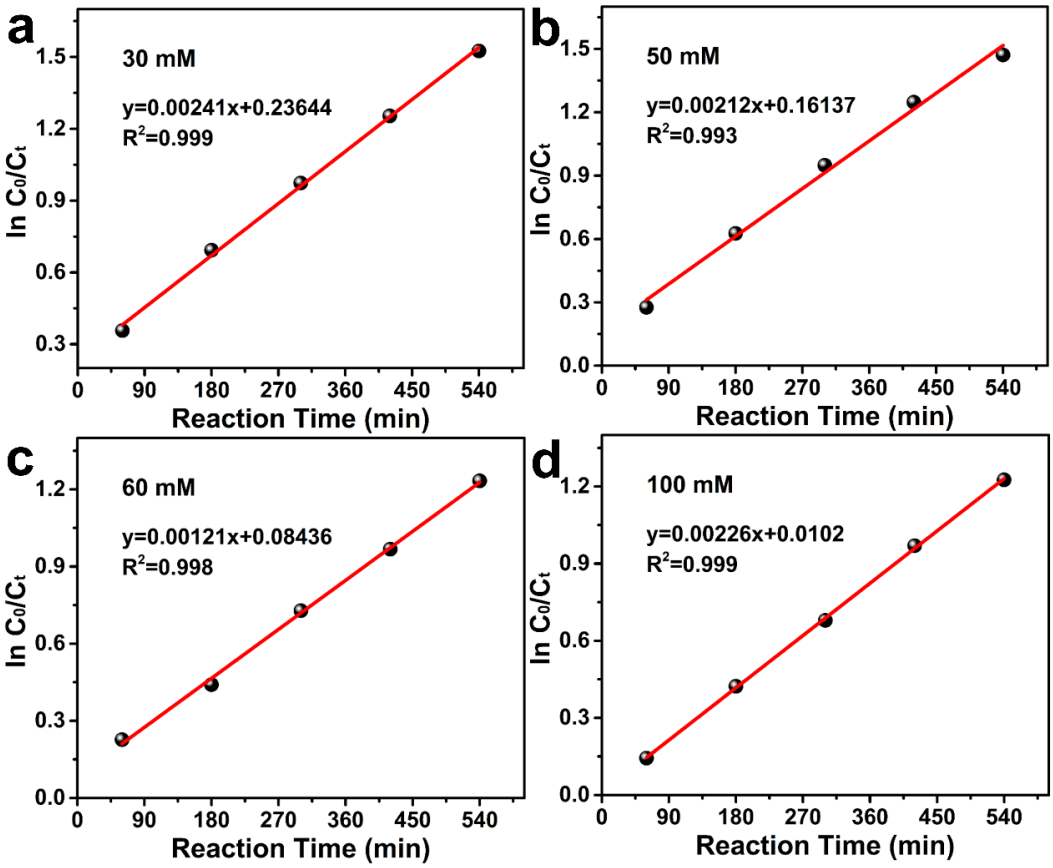

Figure S41. Linear fitting plots of $\ln C_0/C_t$ *vs*. reaction time t based on the pseudo first order kinetic equation for the pristine sample of Fe_3C/NC with different initial nitrate concentrations in the electrolytes at -0.5 V vs. RHE. (a) 30 mM, (b) 50 mM, (c) 60 mM, (d) 100 mM.

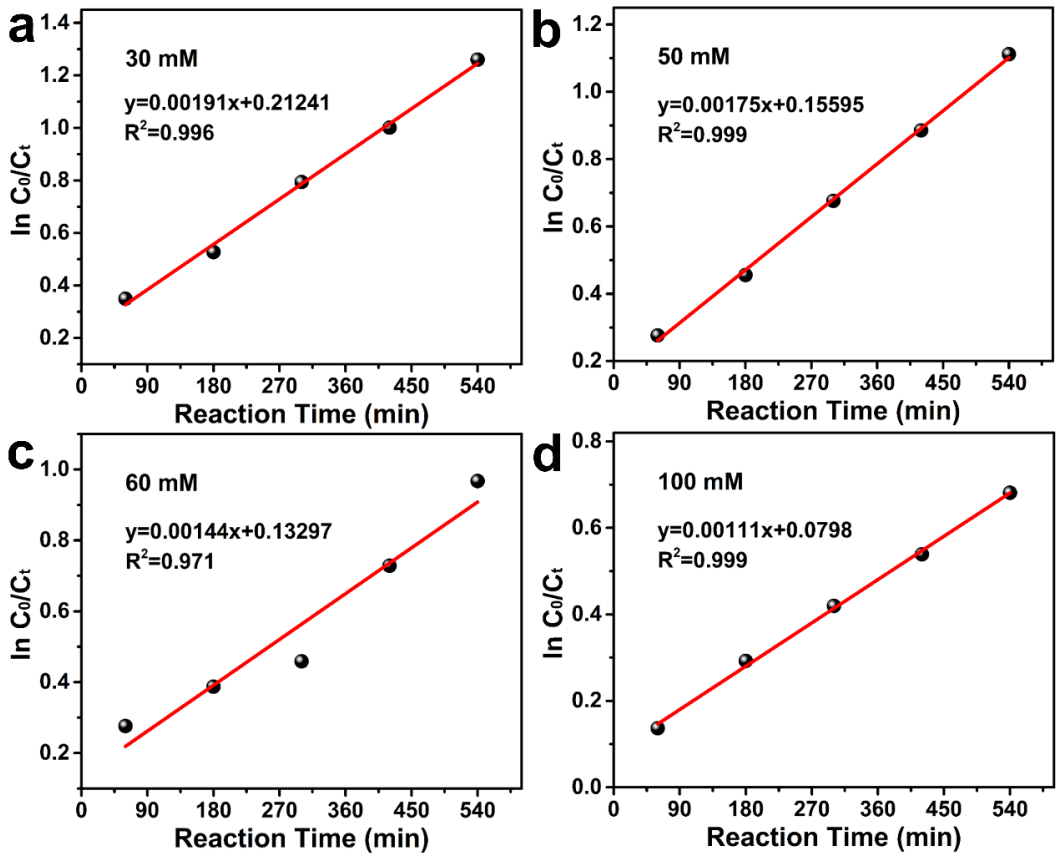

Figure S42. Linear fitting plots of $\ln C_0/C_t$ vs. reaction time t based on the pseudo first order kinetic equation for Air-200 with different initial nitrate concentrations in the electrolytes at -0.5 V vs. RHE. (a) 30 mM, (b) 50 mM, (c) 60 mM, (d) 100 mM.

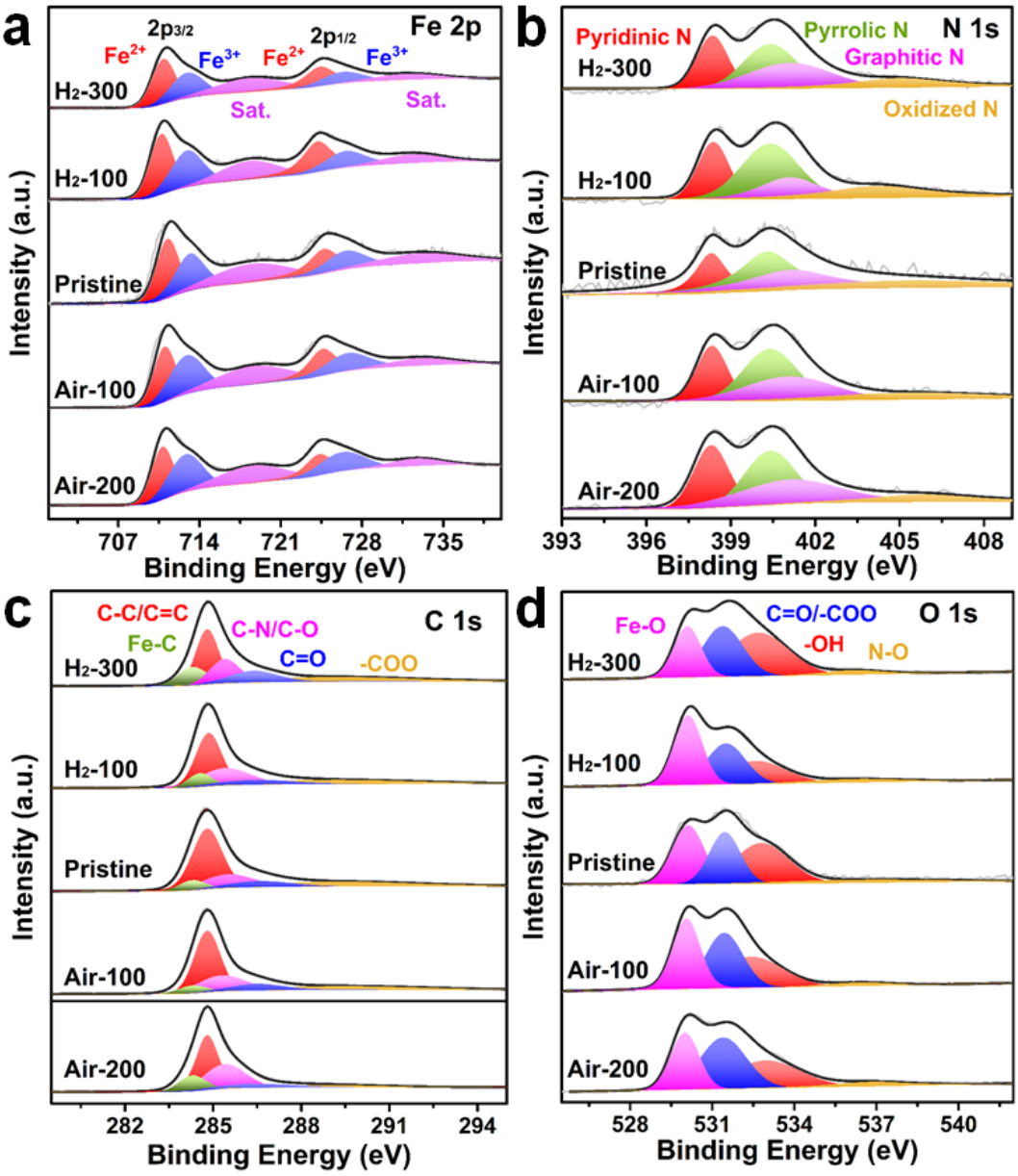

Figure S43. Fe 2p (a), C 1s (b), N 1s (c) and O 1s (d) XPS for the pristine sample of Fe_3C/NC and the control samples of H_2-300, H_2-100, Air-100 and Air-200.

Table S6. The ratio of Fe^{3+}/Fe^{2+} obtained by XPS analysis.

Sample	Fe^{2+} $2p_{3/2}$	$Fe^{3+}2p_{3/2}$	$Fe^{2+}2p_{1/2}$	$Fe^{3+}2p_{1/2}$	Fe^{3+}/Fe^{2+}
H_2-300	0.237	0.193	0.178	0.106	0.720
H_2-100	0.218	0.209	0.196	0.127	0.812
Pristine	0.195	0.192	0.157	0.127	0.908
Air-100	0.194	0.219	0.156	0.153	1.050
Air-200	0.207	0.229	0.136	0.154	1.118

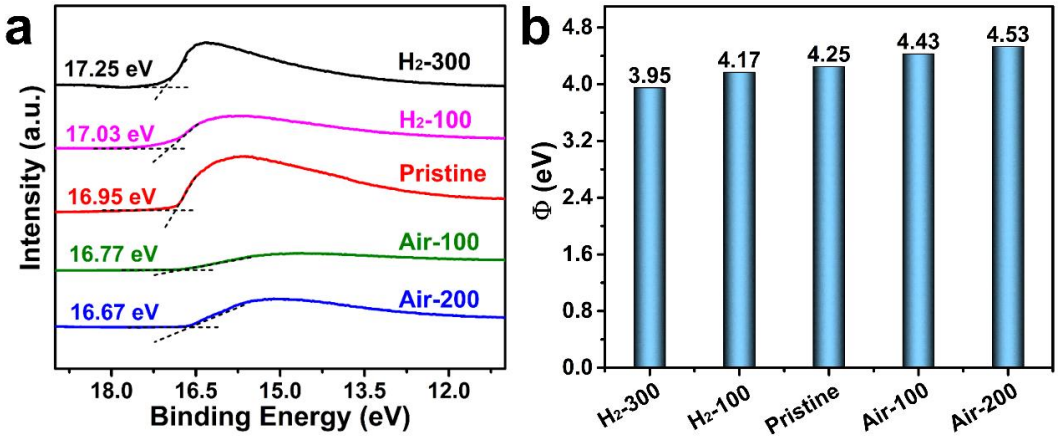

Figure S44. Secondary electron cutoff regions of UPS for Air-200, Air-100, pristine sample of Fe_3C/NC, H_2-100 and H_2-300 (a) and the corresponding work functions (Φ, b).

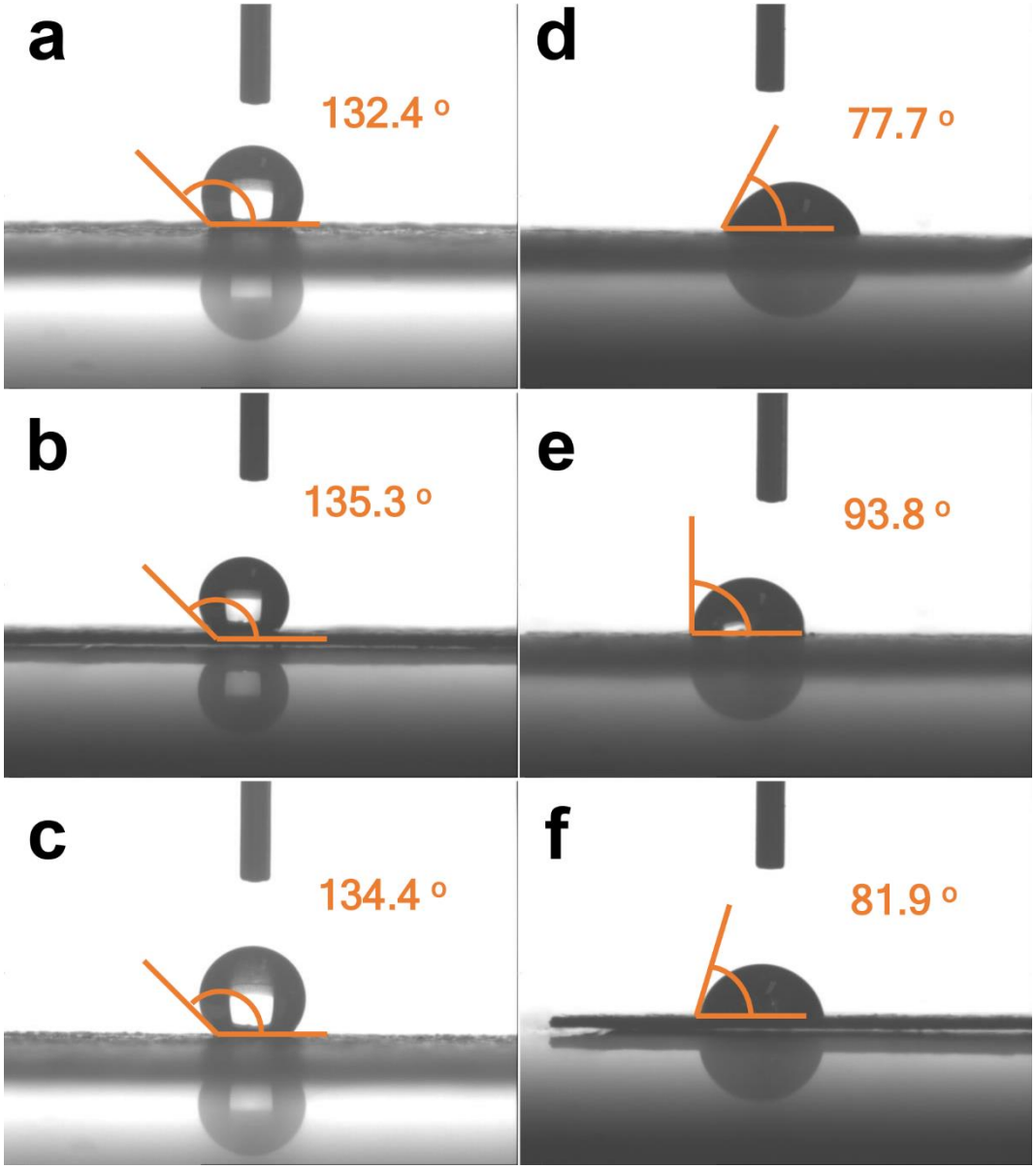

Figure S45. Contact angles for H_2-300 (a, d), Fe_3C/NC (b, e) and Air-200, (c, f) before (a-c) and after (d-f) chronamperometric electrolysis at -0.5 V vs. RHE for 1 h.

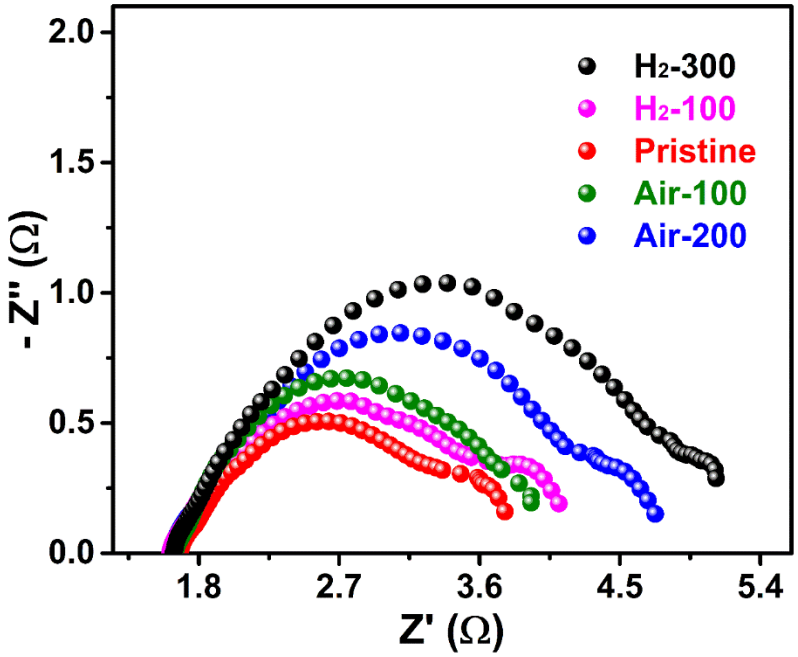

Figure S46. Nyquist plots for Air-200, Air-100, H_2-100, H_2-300 and the pristine sample of Fe_3C/NC at -0.5 V vs. RHE in the frequency range from 0.1 Hz to 100 kHz with an amplitude of 0.05 V.

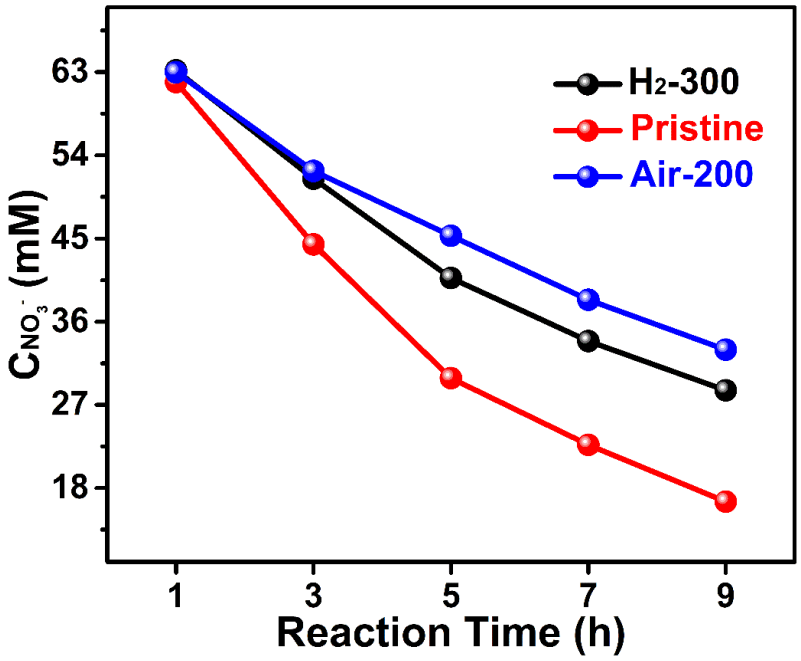

Figure S47. Time-dependent concentrations of nitrate ions in the electrolytes for H_2-300, Air-200 and the pristine sample of Fe_3C/NC after electrolysis at -0.5 V vs. RHE in 1 M KOH and 75 mM KNO_3 for 1 h. .

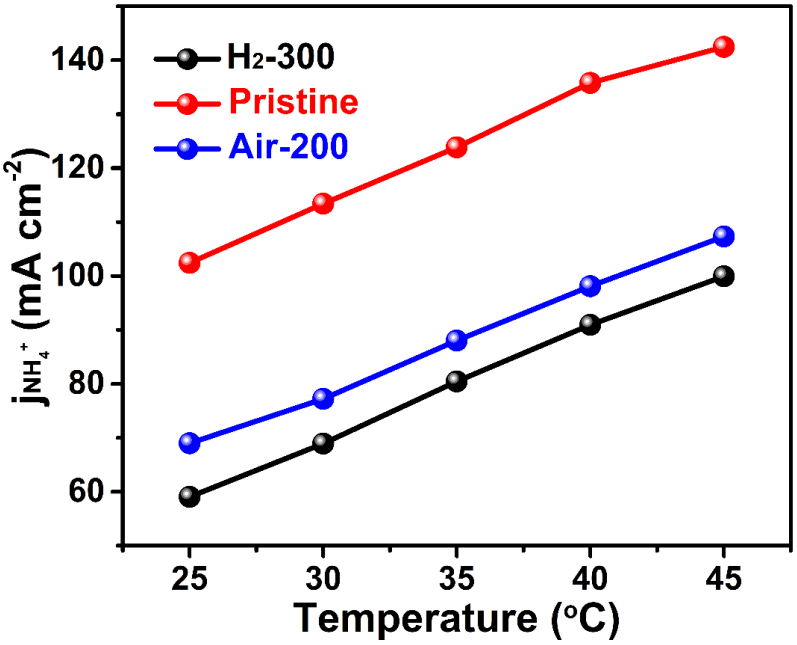

Figure S48. Temperature-dependent partial current densities of ammonium for H_2-300, Air-200 and the pristine sample of Fe_3C/NC after electrolysis at -0.5 V vs. RHE in 1 M KOH and 75 mM KNO_3 for 1 h.

Table S7. Comparison of ammonia yield and selectivity from nitrate electroreduction over Fe_3C/NC with literature results.

Catalyst	Electrolyte	Selectivity (%)	Yield (mmol h^{-1} cm^{-2} / mmol h^{-1} mg^{-1})	Potential (V)	Ref.
Fe_3C/NC	**1 M KOH + 75 mM NO_3^-**	**86.5**	**0.4760/1.1900**	**-0.50** [a]	**This work**
Cu/Cu_2O NWs	0.5 M Na_2SO_4 + 3.2 mM NO_3^-	81.2	0.2449/-	-0.85 [a]	1
TiO_{2-x}	0.5 M Na_2SO_4 + 0.8 mM NO_3^-	87.1	0.0225/0.0450	-1.60 [b]	2
nZVI/BC12	groundwater + 0.8 mM NO_3^-	39.5	0.0010/-	-0.21 [a]	3
FeN-NC-140	0.1 M Na_2SO_4 + 1.6 mM NO_3^-	< 10.0	0.0001/0.00004	-1.30 [b]	4
nZVI@OMC-400	0.02 M NaCl + 3.2 mM NO_3^-	26.0	0.0011/-	-1.30 [b]	5
$Fe^0@Fe_3O_4$	0.4 M NaCl + 0.8 mM NO_3^-	< 20.0	0.0009/-	5 [c]	6
FeNC/MC	0.1 M Na_2SO_4 + 3.2 mM NO_3^-	19.0	0.0005/-	-1.30 [b]	7
Co_3O_4-TiO_2/Ti	0.1 M Na_2SO_4 + 0.8 mM NO_3^-	24.0	0.0008/-	-10 [c]	8
Fe/Cu Composite	0.05 M Na_2SO_4 + 1.6 mM NO_3^-	70.0	0.0600/-	-25 [c]	9
Fe/Fe_3C-NCNF-2	1.6 mM NO_3^-+0.01 M Na_2SO_4	68.0	0.0015/0.0004	-1.30 [b]	10
$Sn_{0.8}Pd_{0.2}$/SS	0.1 M $HClO_4$ + 8 mM NO_3^-	14.0	0.0013/-	-40 [c]	11
Co_3O_4	1600 mM NO_3^- + 0.1 M K_2SO_4	33.6	0.8540/-	-0.65 [a]	12
Bi_2O_3/CC	0.5 M Na_2SO_4 + 0.8 mM NO_3^-	80.3	0.0027/-	-10 [c]	13
PdCu@OMC	0.1 M Na_2SO_4 + 8 mM NO_3^-	24.5	0.0053/	-1.30 [b]	14
$P_{2.1}$-Co_3O_4	0.5 M Na_2SO_4 + 0.8 mM NO_3^-	80.0	0.0005/-	-1.30 [b]	15
Cu/rGO/GP	20 mM NaCl + 20 mM NO_3^-	19.4	0.0145/-	-1.40 [b]	16
$Cu_{49}Fe_1$	0.1 M K_2SO_4 + 3.2 mM NO_3^-	86.8	0.2300/-	-0.70 [a]	17
Ru-ST-12	1M KOH + 100 mM KNO_3	99.0	1.1700/5.56	-0.20 [a]	18
Cu NS	1M KOH +10 mM KNO_3	99.7	0.4000/0.0229	-0.15 [a]	19
Co/CoO NAs	0.1 M Na_2SO_4 + 3.2 mM NO_3^-	91.2	0.1940/-	-1.30 [b]	20
$Pd_{10\%}$-$Cu_{2.5\%}$/CeO_2	0.05 M Na_2SO_4 + 0.8 mM NO_3^-	37.0	0.0019/-	-5 [c]	21
$Pd_{0.4}Cu_{0.6}$	0.01 M $NaClO_4$ + 0.8 mM NO_3^-	49.0	0.0002/-	-0.3 [b]	22
CL-Fe@C	0.1 M Na_2SO_4 + 1.6 mM NO_3^-	58.0	0.0007/0.00018	-1.30 [b]	23
Fe-ppy SACs	0.1 M KOH + 100 mM NO_3^-	98.0	0.1618/0.6738	-0.70 [a]	24
Fe SAC	0.1 M Na_2SO_4 + 500 mM NO_3^-	69.0	0.4600/1.1765	-0.66 [a]	25

[a] The numbers were potentials relative to the reversible hydrogen electrode (RHE).

[b] The numbers were potentials relative to the saturated calomel electrode (SCE).

[c] The numbers were current densities (mA cm^{-2}) at which the constant current electrolysis were performed and the performances were assessed.

Reference

1 Y. Wang, W. Zhou, R. Jia, Y. Yu and B. Zhang, *Angew. Chem. Int. Ed.*, 2020, **59**, 5350-5354.

2 R. Jia, Y. Wang, C. Wang, Y. Ling, Y. Yu and B. Zhang, *ACS Catal.*, 2020, **10**, 3533-3540.

3 A. Wei, J. Ma, J. Chen, Y. Zhang, J. Song and X. Yu, *Chem. Eng. J.*, 2018, **353**, 595-605.

4 J. Wang, L. Ling, Z. Deng and W.-x. Zhang, *Sci. Bull.*, 2020, **65**, 926-933.

5 W. Teng, N. Bai, Y. Liu, Y. Liu, J. Fan and W.-x. Zhang, *Environ. Sci. Technol.*, 2018, **52**, 230-236.

6 Z. A. Jonoush, A. Rezaee and A. Ghaffarinejad, *J. Clean. Prod.*, 2020, **242**, 118569.

7 W. Teng, J. Fan and W.-x. Zhang, *ACS Appl. Mater. Interfaces*, 2020, **12**, 28091-28099.

8 J. Gao, B. Jiang, C. Ni, Y. Qi, Y. Zhang, N. Oturan and M. A. Oturan, *Appl. Catal. B: Environ.*, 2019, **254**, 391-402.

9 Y. Zhang, Y. Zhao, Z. Chen, L. Wang, L. Zhou, P. Wu, F. Wang and P. Ou, *J. Electrochem. Soc.*, 2018, **165**, E420-E428.

10 Y. Lan, J. Chen, H. Zhang, W.-x. Zhang and J. Yang, *J. Mater. Chem. A*, 2020, **8**, 15853-15863.

11 J. F. Su, W.-F. Kuan, H. Liu and C. P. Huang, *Appl. Catal. B: Environ.*, 2019, **257**, 117909.

12 Y. Wang, Y. Yu, R. Jia, C. Zhang and B. Zhang, *Natl. Sci. Rev.*, 2019, **6**, 730-738.

13 M. Chen, J. Bi, X. Huang, T. Wang, Z. Wang and H. Hao, *Chemosphere*, 2021, **278**, 130386.

14 J. Fan, H. Xu, M. Lv, J. Wang, W. Teng, X. Ran, X. Gou, X. Wang, Y. Sun and J. Yang, *New J. Chem.*, 2017, **41**, 2349-2357.

15 J. Gao, B. Jiang, C. Ni, Y. Qi and X. Bi, *Chem. Eng. J.*, 2020, **382**, 123034.

16 D. Yin, Y. Liu, P. Song, P. Chen, X. Liu, L. Cai and L. Zhang, *Electrochimica Acta*, 2019, **324**, 134846.

17 C. Wang, Z. Liu, T. Hu, J. Li, L. Dong, F. Du, C. Li and C. Guo, *ChemSusChem*, 2021, **14**, 1825-1829.

18 J. Li, G. Zhan, J. Yang, F. Quan, C. Mao, Y. Liu, B. Wang, F. Lei, L. Li, A. W. M. Chan, L. Xu, Y. Shi, Y. Du, W. Hao, P. K. Wong, J. Wang, S.-X. Dou, L. Zhang and J. C. Yu, *J. Am. Chem. Soc.*, 2020, **142**, 7036-7046.

19 X. Fu, X. Zhao, X. Hu, K. He, Y. Yu, T. Li, Q. Tu, X. Qian, Q. Yue, M. R. Wasielewski and Y. Kang, *Appl. Mater. Today*, 2020, **19**, 100620.

20 Y. Yu, C. Wang, Y. Yu, Y. Wang and B. Zhang, *Sci. China Chem.*, 2020, **63**, 1469-1476.

21 C. Chen, H. Zhang, K. Li, Q. Tang, X. Bian, J. n. Gu, Q. Cao, L. Zhong, C. K. Russell, M. Fan and J. Jia, *J. Catal.*, 2020, **392**, 231-243.

22 J. F. Su, I. Ruzybayev, I. Shah and C. P. Huang, *Appl. Catal. B: Environ.*, 2016, **180**, 199-209.

23 L. Su, D. Han, G. Zhu, H. Xu, W. Luo, L. Wang, W. Jiang, A. Dong and J. Yang, *Nano Lett.*, 2019, **19**, 5423-5430.

24 P. Li, Z. Jin, Z. Fang and G. Yu, *Energy Environ. Sci.*, 2021, **14**, 3522-3531.

25 Z.-Y. Wu, M. Karamad, X. Yong, Q. Huang, D. A. Cullen, P. Zhu, C. Xia, Q. Xiao, M. Shakouri, F.-Y. Chen, J. Y. Kim, Y. Xia, K. Heck, Y. Hu, M. S. Wong, Q. Li, I. Gates, S. Siahrostami and H. Wang, *Nat. Commun.*, 2021, **12**, 2870.